

Characterization of the immune cell function landscape in head and neck squamous carcinoma to assist in prognosis prediction and immunotherapy

Wenlun Wang^{1,2,3}, Zhouyi Zhang^{1,2}, Wenming Li^{1,2}, Dongmin Wei^{1,2}, Jianing Xu^{1,2}, Ye Qian^{1,2}, Shengda Cao^{1,2}, Dapeng Lei^{1,2}

¹Department of Otorhinolaryngology, Qilu Hospital of Shandong University, Jinan, Shandong, P.R. China

²NHC Key Laboratory of Otorhinolaryngology, Shandong University, Jinan, Shandong, P.R. China

³Key Laboratory for Experimental Teratology of the Ministry of Education and Department of Pathology, School of Basic Medical Sciences, Cheeloo College of Medicine, Shandong University, Jinan, Shandong, P.R. China

Correspondence to: Dapeng Lei; email: leidapeng@sdu.edu.cn

Keywords: HNSCC, immune cell function, immunotherapy, tumor microenvironment, immunophenotype

Received: June 27, 2023

Accepted: October 3, 2023

Published: November 10, 2023

Copyright: © 2023 Wang et al. This is an open access article distributed under the terms of the [Creative Commons Attribution License](https://creativecommons.org/licenses/by/4.0/) (CC BY 4.0), which permits unrestricted use, distribution, and reproduction in any medium, provided the original author and source are credited.

ABSTRACT

Background: The malignant characteristics of cancer depend not only on intrinsic properties of cancer cells but also on the functions of infiltrating immune cells. In this study, we aimed to investigate the functional landscape of immune cells in head and neck squamous cell carcinoma (HNSCC).

Methods: We employed single-sample gene set enrichment analysis to examine the immunophenotypes of HNSCC based on 29 immune cell functions (ICFs) in TCGA and GSE65858 datasets. We analyzed the clinical features, immune microenvironment, molecular profiles, and biological processes. Additionally, we developed and validated an ICF-based risk score for personalized prognosis prediction. We confirmed the value of the ICF score in our cohort using qRT-PCR and immunohistochemistry. Molecular docking was used to predict potential compounds for immunotherapy.

Results: Three immunophenotypes (Immune-L, Immune-M, and Immune-H) were identified in 769 HNSCC samples. The characteristics of Immune-H were consistent with a “Hot” tumor, Immune-L was similar to a “Cold” tumor, and Immune-M exhibited intermediate features. The ICF risk score was associated with immune checkpoints, infiltrating immune cells, tumor mutation burden, and sensitivities to targeted/chemotherapeutic agents. Gene set variation analysis implicated the involvement of metabolic reprogramming pathways in the high-risk group. The combination of “Tumor Immune Dysfunction and Exclusion” and “Immunophenoscore” algorithms indicated that the low-risk group had a higher likelihood of benefiting from immunotherapy. Finally, we identified Eltrombopag and other compounds that may be beneficial for HNSCC immunotherapy.

Conclusion: Our study provides a novel perspective on the tumor microenvironment of HNSCC, aiding in the understanding of HNSCC heterogeneity and the development of personalized/precision medicine.

INTRODUCTION

Head and neck squamous cell carcinoma (HNSCC) is one of the most aggressive malignant cancers with

a high risk of metastasis and mortality [1]. It is estimated that there were approximately 878,348 new cases and 444,347 deaths globally in 2020 [2]. Over the past few decades, the introduction of immune

checkpoint inhibitors (ICIs) has revolutionized the treatment approach and prognosis for advanced HNSCC patients [3]. However, the objective response rate to ICIs in recurrent or metastatic HNSCC remains relatively low, ranging from 13% to 18% [4, 5].

Although programmed death ligand-1 (PD-L1) has been established as a biomarker for immune checkpoint inhibitors (ICIs) in HNSCC, its limitations have been recognized, as some PD-L1-negative patients still derive benefit from ICIs [6]. Recent studies have proposed that the tumor microenvironment (TME) holds promise as a source of biomarkers for immunotherapy [7, 8]. The malignant phenotype of tumors was influenced not only by inherent characteristics of cancer cells but also by components of the TME [9, 10]. For instance, CD8⁺ T cells could be present in both “inflamed” and “immune-excluded” tumors [11]. However, in “immune-excluded” tumors, CD8⁺ T cells were unable to mount an effective immune response against the tumor, potentially due to matrix barriers, T cell exhaustion, and deficiencies in immune factors. Despite HNSCC exhibiting a higher infiltration of immune cells compared to other tumor types, its prognosis remains poor [12]. Hence, further investigations are necessary to unravel the functional status of immune cells in the TME of HNSCC.

Consequently, the objective of this study was to investigate the TME in HNSCC based on the immune cell function, elucidate potential molecular mechanisms, and predict prognosis as well as the responsiveness to immunotherapy in HNSCC.

MATERIALS AND METHODS

Data collection

We downloaded transcriptome data (FPKM) and clinical information of 499 HNSCC patients from The Cancer Genome Atlas (TCGA) database. The sequencing platform was Illumina HiSeq. GRCh38 was used for gene annotation.

Transcriptome and clinical data of 270 HNSCC patients were collected from the GEO database (GSE65858). Raw data was extracted using Illumina GenomeStudio, and then log₂-transformed and normalized using the Robust Spline Normalization (RSN) method. The annotation platform was GPL10558.

The study was conducted in accordance with the principles outlined in the Declaration of Helsinki and was approved by the Ethics Committee of Qilu Hospital

of Shandong University (KYL-2020(KS)-320). All patients enrolled from our institution provided written informed consent.

Identification of the immunophenotype based on immune cell function (ICF)

In this study, we employed the immune gene set previously reported by He et al. [13]. This gene set consists of 29 gene signatures associated with immune cell types, functions, and signaling pathways (Supplementary Table 1). To estimate the enrichment scores of these 29 gene signatures in HNSCC samples, we utilized ssGSEA (single sample gene set enrichment analysis). Subsequently, the HNSCC samples were clustered into different immunophenotypes using the “Rtsne” package based on these 29 gene signatures.

The “survival” package was used to conduct Kaplan-Meier survival analysis and log-rank test according to the immunophenotypes.

Analysis of immune microenvironment characteristics and functional enrichment

The “ESTIMATE” package was employed to evaluate the stromal score, immune score, and tumor purity. Furthermore, the infiltration of 22 immune cells was determined using the “CIBERSORT” package. To compare the expression of immune-related genes among different groups, the “limma”, “ggplot2”, and “ggpubr” packages were utilized, employing the Wilcoxon test. Gene set enrichment analysis (GSEA) was performed using the “enrichplot” and “clusterProfiler” packages to compare the enrichment of functional pathways between different immunophenotypes.

WGCNA (weighted gene co-expression network analysis)

The “WGCNA” package was used to develop the gene co-expression network. The soft threshold $\beta = 8$ was determined as the optimal power value. We set the minimum number of genes in each module to be greater than 60. The gene topology matrix was constructed by using the dynamic cut tree algorithm. The final result was obtained by merging modules with a similarity ≥ 0.75 . The correlation between gene modules and clinical traits was determined by the module significance. Genes with weight > 0.3 in the module were screened to develop a protein-protein interaction (PPI) network by using the STRING platform. The hub genes of the PPI network were determined by 12 algorithms from cytoHubba plugin of Cytoscape.

The “clusterProfiler” package was used to conduct GO and KEGG enrichment analysis for module genes, with a significance level of $P < 0.01$.

Construction and validation of the ICF gene signature

We utilized the “limma” package to analyze the differentially expressed genes (DEGs), and obtained the immune-related gene list from the IMMPORT database. The intersection of the two gene lists yielded immune-related differentially expressed genes (IRDEGs). Next, univariate survival analysis was conducted to select prognosis-related immune genes (PIGs) using the “survival” package.

The “glmnet” package was employed to conduct lasso regression analysis and establish an ICF gene signature. For conducting univariate and multivariate survival analysis, we employed the “survival” package.

Construction and validation of the ICF score nomogram

We utilized the “survminer” package to construct the nomogram, and considered factors with $p < 0.05$ as statistically significant. Additionally, we drew ROC and calibration curves to evaluate the performance of the model.

Analysis of potential transcription factors (TFs) for PIGs

To explore possible TFs for PIGs, we obtained tumor-associated TFs from the Cistrome database (<http://www.cistrome.org/>). TFs and PIGs with co-expression relationships were selected according to $|\text{pearson correlation coefficient}| > 0.4$ and $\text{FDR} < 0.01$. The correlation of TFs and PIGs was summarized into an alluvial diagram using the “ggalluvial” package. The STRING platform was used to construct the PPI network.

Integrative analysis of gene set variation analysis (GSVA), tumor mutation burden (TMB), and cancer stem cell index

GSVA is a nonparametric unsupervised clustering method that can analyze specific gene sets in a single sample, thus enabling “pathway” level difference analysis. We utilized the “GSVA” package to evaluate the enrichment of 186 KEGG gene sets. Pathways with $P < 0.05$ and $\log_{2}\text{FC} > 0.1$ were considered significantly enriched.

We collected mutation information from the TCGA data portal. The “maftool” package was used to investigate

comprehensive somatic variants. We employed the chi-square test to compare mutation frequencies across different groups.

Tathiane et al. used machine learning algorithms to analyze the multi-omics features of embryonic stem cells [14]. This method was utilized to calculate the stem cell indexes of TCGA HNSCC. The correlation between mRNA stemness index (mRNAsi) and ICF risk score was evaluated by “limma” package.

Analysis of treatment sensitivities

The “pRRophetic” package was employed to estimate the IC50 values of 251 chemotherapeutic/targeted agents in HNSCC patients [15]. The Tumor Immune Dysfunction and Exclusion (TIDE) platform was used to calculate T-cell dysfunction and exclusion scores [16]. A higher TIDE score indicated a greater potential for tumor immune escape and might result in poorer immunotherapy efficacy. Pornpimol et al. developed the immunophenoscore (IPS) based on factors influencing tumor immunogenicity [17]. IPS has been proved to be an ideal predictor for ICIs responsiveness. An increased IPS value was indicative of a higher likelihood of benefiting from ICIs.

Identification of key targets of ICF gene signature

The STRING platform was employed to develop a PPI network of the ICF gene signature with interaction score ≥ 0.4 . The Cytoscape software was utilized to determine hub genes according to node connectivity.

Molecular docking

The molecular structures of 1379 FDA-approved compounds were obtained from the ZINC15 database (<https://zinc15.docking.org/>). The 3D structure of CD247 was collected from the PDB database (<http://rcsb.org/>). Firstly, “AutoDockTools-1.5.7” was used to process the structure of the protein, including adding hydrogens, removing the water, and adding the Gasteiger charges. Due to the small molecular weight of CD247 protein, global docking was performed. Small molecules were batch processed by “Obabel” and converted to pdbqt format. Finally, “Vina” was used for batch docking, and the default parameters were adopted.

In vitro validation and survival analyses

Between 2016 and 2017, a total of 80 patients who underwent surgical treatment and were pathologically confirmed to have HNSCC were randomly selected from Qilu Hospital. These patients were followed up until December 2022. Total RNA was extracted from

frozen tumor tissues or cultured cells using TRIzol reagent from Absin, China. The cDNA was synthesized using the PrimeScript RT kit from Takara, Japan. RT-PCR was performed using the TB Green Premix Ex Taq II kit, also from Takara, Japan. The primer sequences used are provided in Supplementary Table 2, and GAPDH was used as an internal control. The relative mRNA levels were calculated using the $2^{-\Delta\Delta C_t}$ method.

A paraffin-embedded specimen from each patient was obtained from the pathology department and subjected to immunohistochemical (IHC) staining using an anti-CD247 antibody (1:200, Abcam, UK). The specimens were scored using a semi-quantitative method as previously described [18]. The staining intensity was categorized as follows: 0 (negative), 1 (weak), 2 (moderate), and 3 (strong). Survival analyses were performed using the “survminer” package.

Cell lines and cell culture

The primary oral mucosal epithelial cells, UMSCC, FaDu, and HN-5 cells were obtained from Meisen Cell Technology Company (China). The cells were maintained in a humidified incubator with 5% CO₂ at 37°C while being cultured in DMEM medium (HyClone, USA) supplemented with 10% fetal bovine serum (PAN, Germany), 100 U/mL penicillin, and 100 µg/mL streptomycin. The methods for quantitative real-time PCR have been described above.

RESULTS

Identification of the ICF immunophenotype and analysis of the immune microenvironment landscape

We used ssGSEA to assess infiltration levels of 29 functional immune cells in HNSCC samples (Supplementary Table 3). The hierarchical cluster analysis of HNSCC was carried out using T-SNE (t-Distributed Stochastic Neighbor Embedding) algorithm. When divided into three clusters, the intra-cluster consistency and inter-cluster discrimination were found to be the highest (Supplementary Figure 1). The heatmap depicted the diverse degrees of infiltration of 29 functional immune cells across the three clusters, ranging from low to high (Figure 1A). As a result, we have designated the three clusters as follows: “Immune-H” to signify the cluster with high immune cell infiltration, “Immune-M” to represent the cluster with moderate immune cell infiltration, and “Immune-L” to indicate the cluster with low immune cell infiltration. The ESTIMATE results showed that the Immune-H subtype exhibited a higher infiltration of immune and stromal cells compared to the Immune-

M and Immune-L subtypes. Correspondingly, the Immune-H subtype had the lowest tumor cell purity. Furthermore, similar immunophenotypes and microenvironment characteristics were also confirmed in GSE65858 (Figure 1C). Survival analysis revealed that the Immune-H subtype had the most favorable survival prognosis of the three subtypes (Figure 1B, 1D).

The CIBERSORT analysis revealed higher fractions of CD8+ T cells, naive B cells, helper follicular T cells, Treg cells, activated CD4+ T cells, M1 macrophages, and resting mast cells in the Immune-H subtype (Figure 1E). On the other hand, the Immune-L subtype showed higher fractions of M0 macrophages, activated dendritic cells, and activated mast cells. The Supplementary Figure 2 and Supplementary Results show the impact of immune cell infiltration on patient survival. GSEA analysis revealed that the Immune-H subtype displayed significant activation of immune rejection and immunodeficiency pathways (Figure 1F). In contrast, except for the chemical carcinogenesis of DNA adducts, no significant enrichment of pathways was observed in the Immune-L subtype (Supplementary Figure 3A, 3B). We also performed WGCNA to identify the immunophenotype-related gene module and hub genes (Supplementary Results and Supplementary Figure 4). Furthermore, it was observed that the expression of HLA alleles increased in correlation with the immune subtypes (Figure 1G). Additionally, the expression of most inhibitory immune checkpoints was found to be elevated in association with the ICF immune subtypes (Figure 1H).

Construction and validation of the ICF gene signature

It is expensive to determine the ICF immunophenotype by analyzing a large amount of genes through ssGSEA. Consequently, we developed an ICF gene signature for individualized prediction. The TCGA-HNSCC database was used as the training set, and GSE65858 served as the validation set (Supplementary Table 4). We identified 1177 DEGs by comparing the Immune-H and Immune-L subtypes. An intersection of DEGs and immune genes from IMMPORT yielded 373 immune-related DEGs (IRDEGs) (Figure 2A, Supplementary Figure 5A, 5B and Supplementary Table 5). Univariate analysis identified 30 genes associated with prognosis (PIGs, Figure 2B), which were used in LASSO analysis to develop the gene signature: Risk score = $CD19 \times (-0.0663) + ZAP70 \times (-0.1933) + TNFRSF4 \times (-0.1303) + CCL22 \times (-0.0038) + RBP5 \times (-0.0244) + STC2 \times (0.1637) + ROBO1 \times (-0.0501) + CTSG \times (-0.1122)$ (Figure 2C). We also investigated the possible transcription factors involved in the regulation of PIGs (Supplementary Results and Supplementary Figure 6).

The patients were stratified into high- and low-risk groups based on the median risk score. The survival analysis showed that the low-risk group had a significantly better survival compared to the high-risk group ($P < 0.01$, Figure 2D, 2E). The area under the curve (AUC) values for the ICF gene signature at 1-

year, 3-year, and 5-year were 0.682, 0.682, and 0.782, respectively (Figure 2F). These AUC values were higher than those reported by Du et al. for their metabolism-related gene signature (AUC at 1-year, 3-year, and 5-year were 0.66, 0.67, and 0.75, respectively) [19]. The calibration curve demonstrated high accuracy

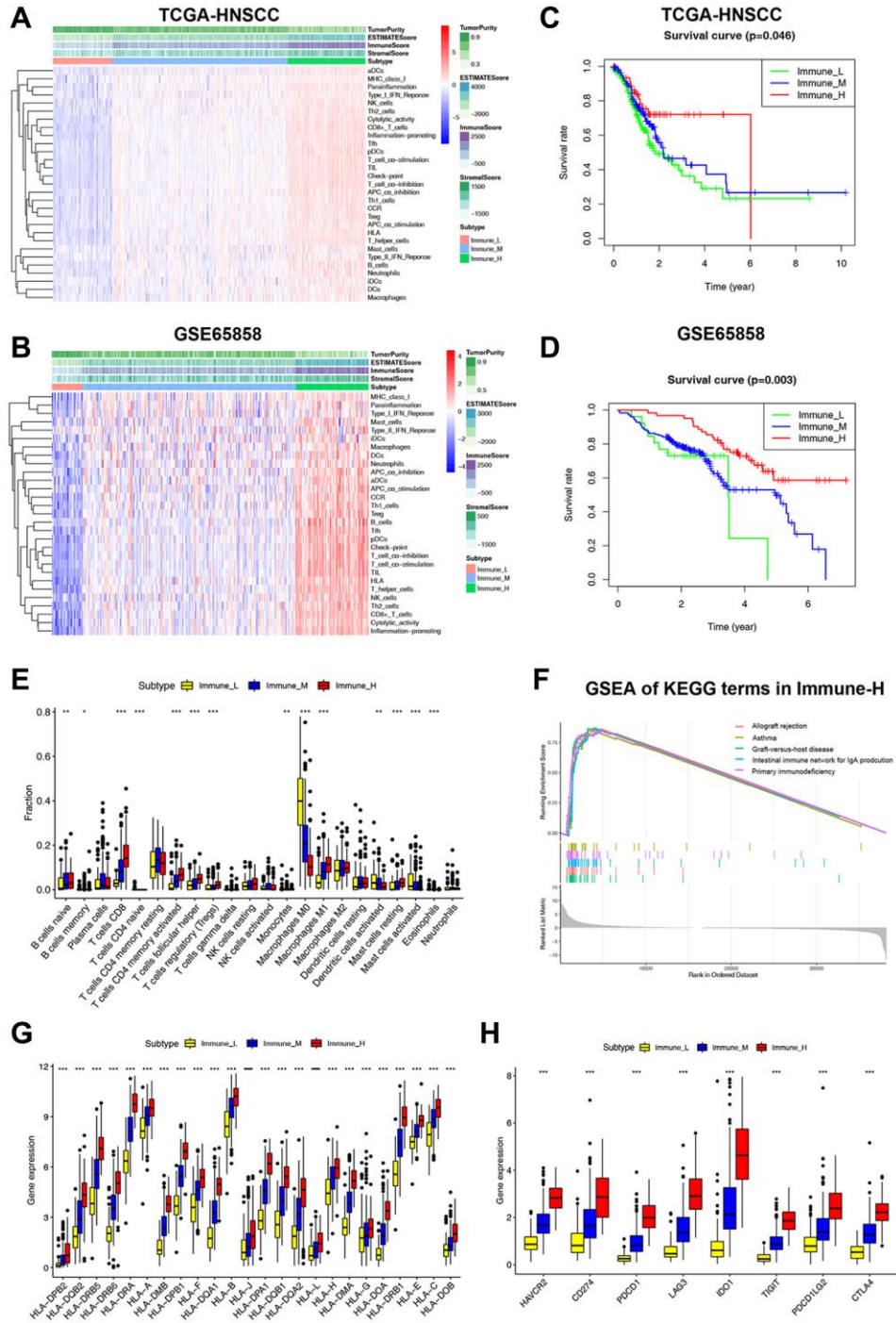


Figure 1. Classification of HNSCC based on ICF and analysis of the immune microenvironment. (A, B) The heatmap shows the enrichment of 29 immune gene signatures and TME components in different ICF subtypes. (C, D) Kaplan-Meier analysis for overall survival of three ICF subtypes. (E) The fractions of immune infiltrating cells in three ICF subtypes. (F) GSEA of KEGG pathways in Immune-H. (G) The expression levels of HLA alleles in different ICF subtypes. (H) The expression levels of immune checkpoints in different ICF subtypes. * $p < 0.05$, ** $p < 0.01$, *** $p < 0.001$.

(Figure 2G). Cox regression analyses revealed that age, tumor stage, and the ICF risk score were independent prognostic factors (Figure 2H). The predictive value of

the ICF gene signature was further confirmed in the GSE65858 dataset (Supplementary Figure 5C–5F). A nomogram was constructed incorporating the ICF risk

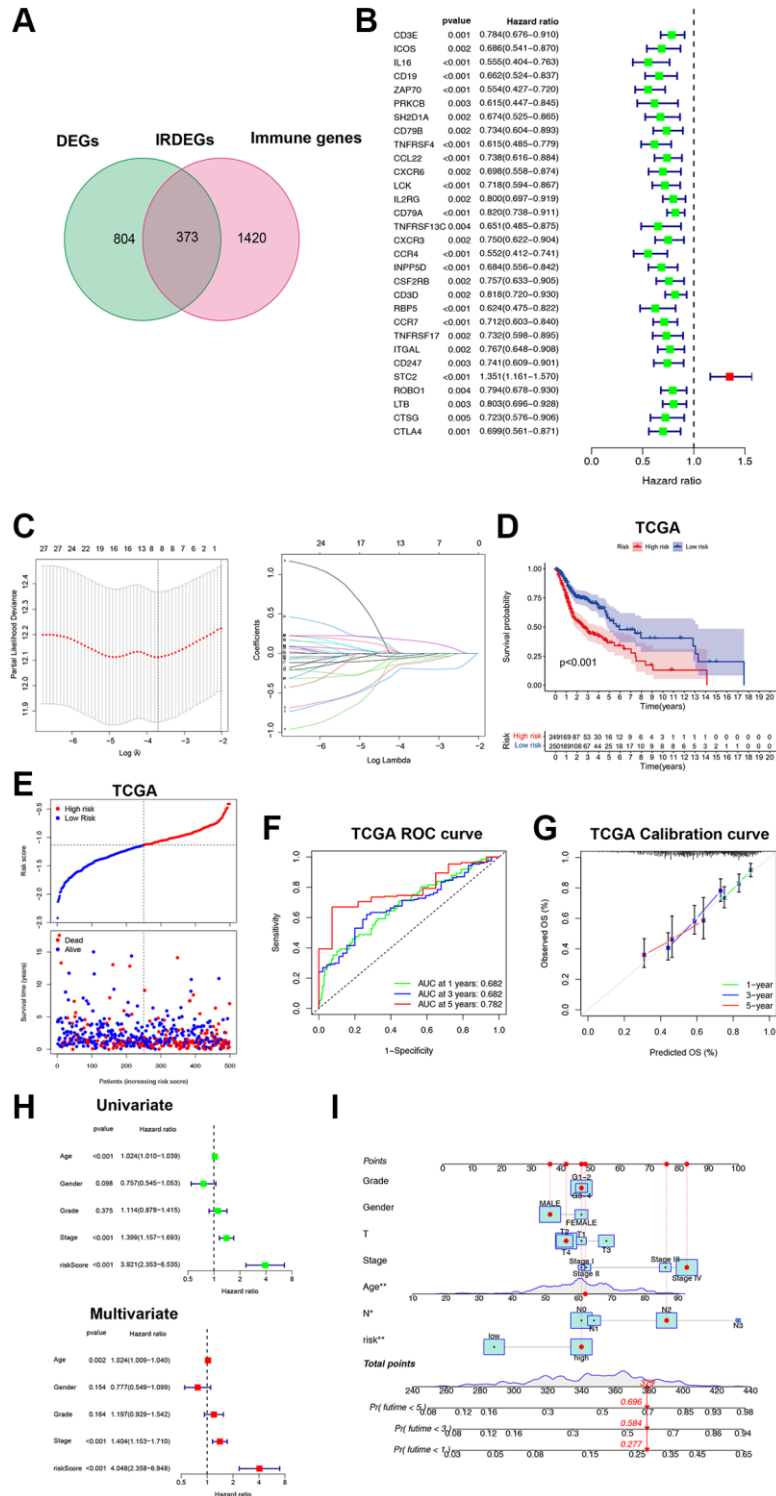


Figure 2. Construction and validation of the ICF gene signature. (A) Venn diagram shows 373 IRDEGs. **(B)** Univariate Cox analysis for PIGs. **(C)** Lasso regression analysis of PIGs. **(D)** Comparison of overall survival between high- and low-risk groups. **(E)** The correspondence between ICF risk scores and survival outcomes in the training set. The ROC curve **(F)** and calibration curve **(G)** of the ICF score for predicting 1-year, 3-year and 5-year survival. **(H)** Univariate and multivariate survival analyses of ICF score and clinical traits. **(I)** Nomogram based on the ICF score and clinical traits for predicting 1-year, 3-year and 5-year survival. * $p < 0.05$, ** $P < 0.01$.

score and clinical characteristics to predict 1-year, 3-year, and 5-year survival (Figure 2I). The AUC values for the nomogram were 0.696, 0.735, and 0.709, respectively (Supplementary Figure 5G). The calibration curve indicated a high level of agreement between the predicted and observed outcomes (Supplementary Figure 5H).

We collected 80 cases of HNSCC from Qilu Hospital of Shandong University. Gene expression levels were quantified using qRT-PCR. The study cohort was divided into a high-risk group ($n = 40$) and a low-risk group ($n = 40$) based on the median ICF risk score. The heatmap of gene enrichment revealed that STC2 was upregulated in the high-risk group, whereas CCL2, CTSG, ROBO1, CD19, RBP5, ZAP70, and TNFRSF4 were highly expressed in the low-risk group (Figure 3A).

Patients in the high-risk group exhibited a significantly lower survival rate compared to those in the low-risk group ($P = 0.045$, Figure 3B). In the stratified survival analysis, STC2 was found to be linked with an unfavorable prognosis in HNSCC patients, whereas CCL2, CTSG, CD19, RBP5, ZAP70, and TNFRSF4 were associated with a favorable prognosis in these patients (Figure 3C).

Characterization of the ICF score in molecule mechanisms and immune microenvironment

GSVA was conducted to investigate the molecular mechanisms (Figure 4A). In the high-risk group, pathways such as the biosynthesis of glycosylphosphatidylinositol-anchored proteins (GPI-APs), protein export, and pentose phosphate were

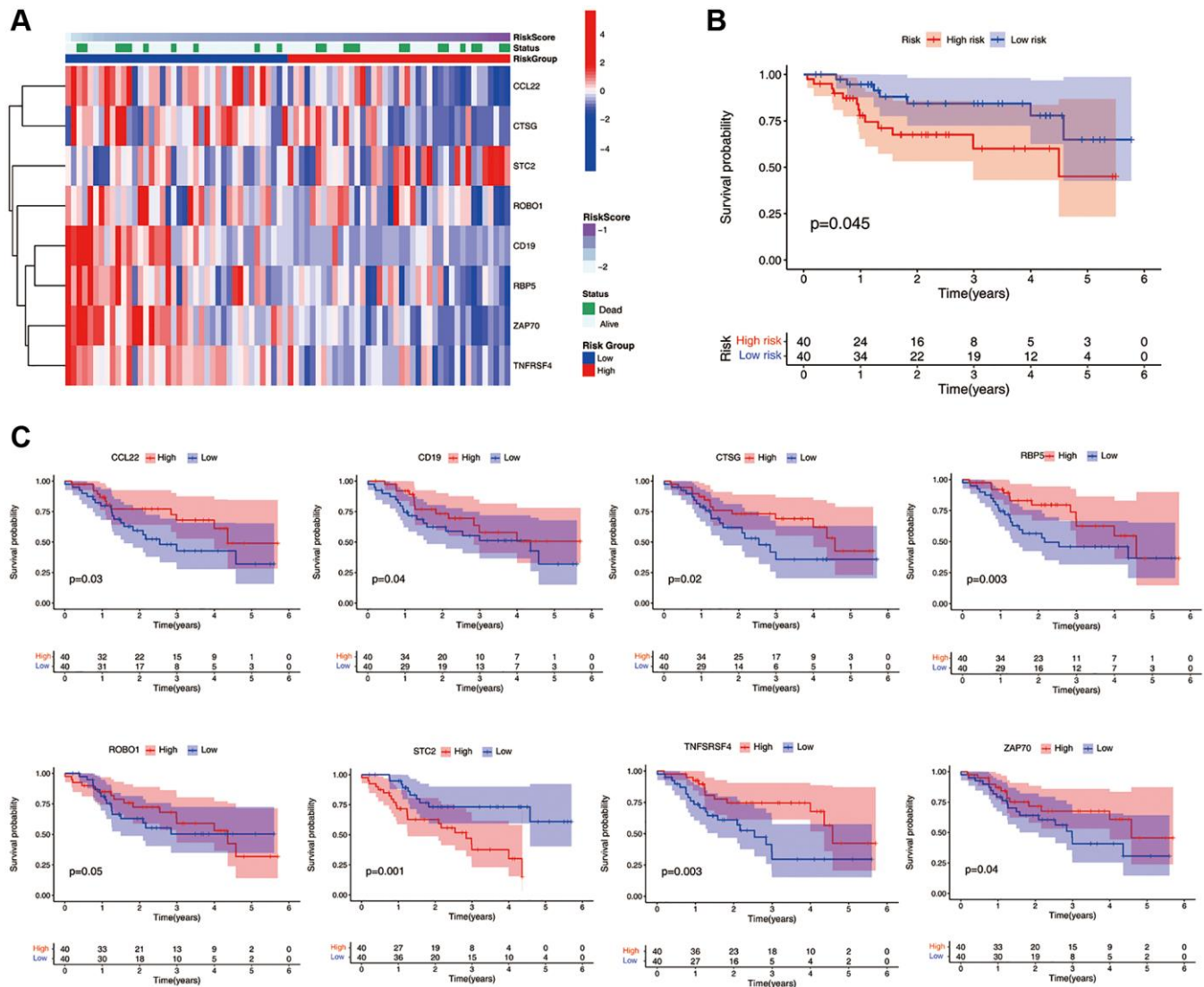


Figure 3. Validation of the ICF gene signature in Qilu cohort. (A) The heatmap illustrates the expression levels of eight ICF signature genes in the Qilu cohort. (B) Kaplan-Meier survival analysis demonstrates the survival outcomes of the high- and low-risk groups in the Qilu cohort. (C) Kaplan-Meier survival analysis stratified by the expression levels of eight ICF signature genes in the Qilu cohort.

significantly enriched. In the low-risk group, pathways of immune activation and immunodeficiency, such as antigen presentation processing and primary

immune deficiency, were significantly enriched. The expression of most inhibitory immune checkpoints was found to be negatively correlated with the ICF score

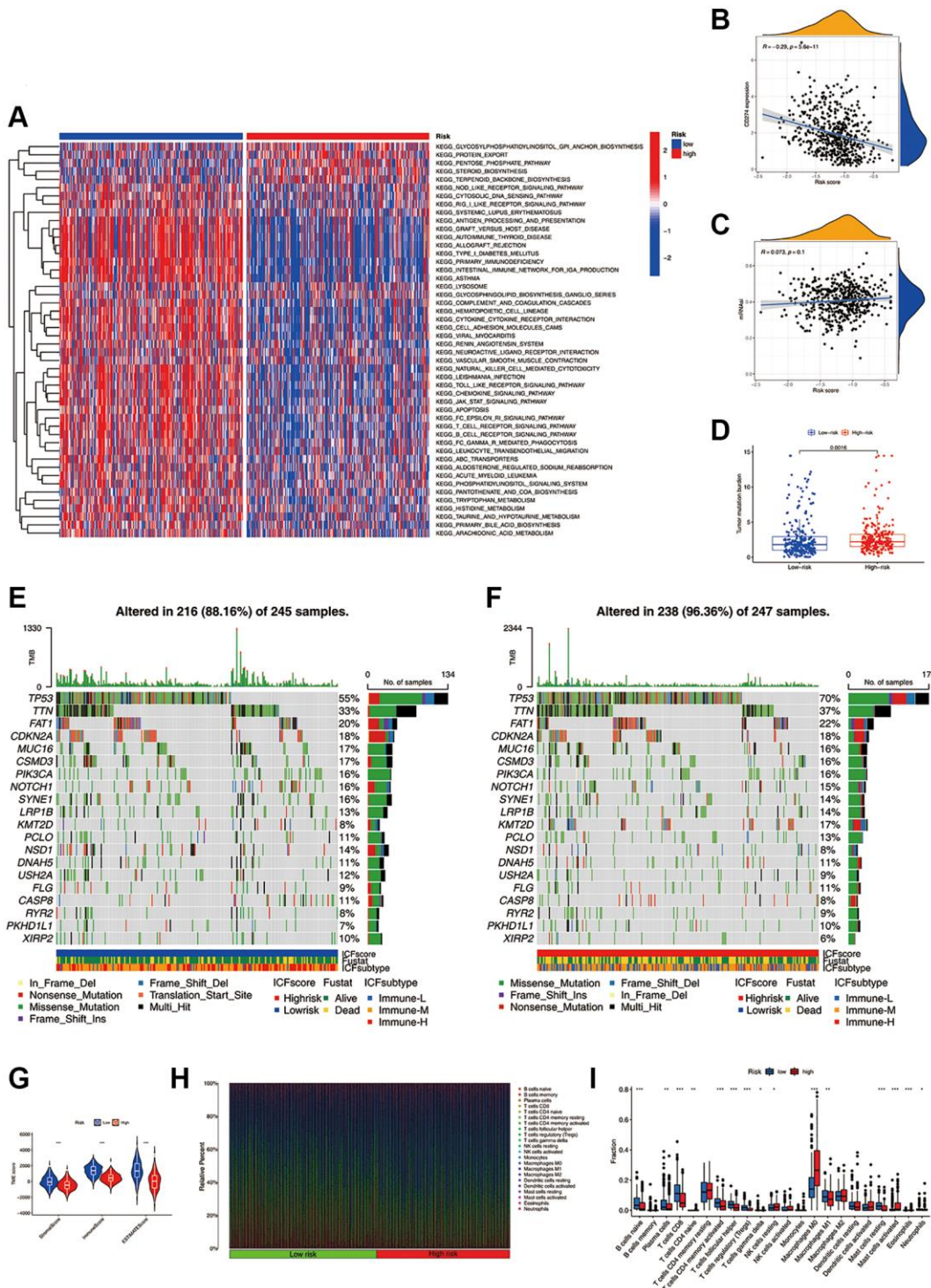


Figure 4. Molecular mechanisms and the TME landscape of different ICF risk groups. (A) GSVA of KEGG pathways in high- and low-risk groups. (B) Correlation of the ICF score and the expression of immune checkpoint CD274 (PD-L1). (C) Correlation of the ICF score and cancer stemness indices (mRNAsi). (D) Comparison of TMB between high- and low- risk groups. The landscape of somatic variance of the low-risk group (E) and high-risk (F) group. (G) Comparisons of TME components between high- and low-risk groups. (H) The bar plot shows the fractions of 22 immune infiltrating cells in high- and low-risk groups. (I) Comparisons of the proportions of 22 immune infiltrating cells between high- and low-risk groups.

(Figure 4B and Supplementary Figure 7). The self-renewal property and therapy resistance of cancer stem cells play a crucial role in the development of malignant tumor phenotypes [14]. However, there was no observed correlation between the ICF score and the cancer stem cell index (Figure 4C). Tumor gene mutation was considered as a prerequisite for immunotherapy. In this study, the high-risk group exhibited a significantly higher TMB compared to the low-risk group (Figure 4D). Survival analysis indicated that the ICF score and TMB had a synergistic effect on prognosis prediction (Supplementary Results and Supplementary Figure 8). Furthermore, somatic variance analysis revealed that the high-risk group had higher frequencies of TP53, KMT2D, and NSD1 mutations compared to the low-risk group (Figure 4E, 4F, and Supplementary Table 6, $p < 0.05$). We have investigated the correlation between the ICF signature genes and the infiltration of immune cells (Supplementary Results and Supplementary Figure 9).

The ESTIMATE algorithm revealed that the high-risk group had lower fractions of immune and stromal components (Figure 4G). According to the CIBERSORT analysis (Figure 4H, 4I), the high-risk group had higher proportions of M0 macrophages, activated mast cells, and resting NK cells. Conversely, the low-risk group had higher fractions of CD8+ T cells, activated CD4+ memory B cells, Treg cells, M1 macrophages, naive B cells, plasma cells, follicular helper T cells, and resting mast cells. We have further compared our ICF immunophenotyping strategy with the previously reported immune typing strategy (Supplementary Results and Supplementary Figure 10).

Evaluation of the ICF score in predicting chemotherapy and immunotherapy

The aforementioned evidence indicated that the ICF score was associated with distinct TME characteristics and biological processes, potentially leading to different therapeutic responses. We further investigated the IC50 values of 251 drugs in HNSCC (Figure 5A). Erlotinib and docetaxel were found to be more effective in the high-risk group, while vinblastine, cyclophosphamide, sunitinib, and rapamycin demonstrated higher sensitivity in the low-risk group. Notably, the sensitivities of commonly used drugs for HNSCC, such as Cisplatin and Bleomycin, did not show significant differences between the high- and low-risk groups (Supplementary Figure 11).

We investigated the utility of the ICF score in predicting immunotherapy response. Figure 5B demonstrated that the low-risk group had significantly lower T-cell exclusion scores, which was consistent

with the higher immune components observed in this group. Additionally, the low-risk group exhibited higher T-cell dysfunction scores and comprehensive TIDE scores, which was in line with the activation of immune deficiency and autoimmune pathways in this population. There was no significant difference in microsatellite instability (MSI) between the high-risk and low-risk groups. Finally, the IPS values showed a significant increase in the low-risk group, indicating that this group may be more responsive to ICIs and more likely to benefit from them (Figure 5C).

Identification of the key target CD247 and prediction of small molecule drugs

Using the STRING platform, we constructed a protein-protein interaction (PPI) network of the ICF gene signature (interaction score ≥ 0.4 , Figure 6A). CD247 was identified as the key target, located at the core of the network. HNSCC cell lines (Fadu, HN-5, and UMSCC) exhibited high expression of CD247 compared to primary oral mucosal epithelial cells (Figure 6B). Immunohistochemical staining was performed on tumor tissues from 80 patients, and the expression of CD247 was scored based on staining intensity (Figure 6C). Our results indicated that patients with high CD247 expression (score 2 and 3) had a more favorable prognosis of survival (Figure 6D), suggesting that CD247 may be a target for tumor immunity in HNSCC and that drugs targeting CD247 could be a potential therapeutic strategy.

In order to identify potential drugs that interact with CD247, we performed molecular docking using over 1300 FDA-approved compounds. Three compounds with the lowest binding energies to CD247 were identified: Eltrombopag (-8.3 kcal/mol, Figure 6E), ZINC116473771 (-8 kcal/mol, Figure 6F), and Conivaptan (-7.8 kcal/mol, Figure 6G). For example, Eltrombopag formed hydrogen bonds with key amino acid residues TYR-12 and VAL-14 in the binding pocket of CD247, indicating a high affinity interaction. The top ten compounds with the highest affinity to CD247 are summarized in Supplementary Table 7. These compounds may be potential immunotherapy drugs for HNSCC.

DISCUSSION

In the past decade, ICIs represented by anti-PD-L1 antibody have greatly improved the prognosis of advanced HNSCC. Consequently, there has been a growing interest in studying the TME of HNSCC. Zhang et al. proposed an immune classification of HNSCC based on matrix and immune scores, providing valuable insights into the immune microenvironment of

HNSCC and its potential implications in immunotherapy [20]. In this study, we identified three immunophenotypes in HNSCC based on 29 functional immune cells. Furthermore, we have utilized a range of methodologies including ssGSEA, WGCNA, GSEA, and GSVA to conduct a comprehensive analysis of the characteristics of the tumor microenvironment (TME). These approaches have allowed us to explore potential molecular mechanisms, establish associations with clinical features, predict prognosis, assess treatment sensitivity, identify key targets, and even predict the efficacy of small molecule drugs.

In our study, the Immune-H subtype exhibited the highest abundance of immune and matrix components within the tumor microenvironment. This subtype was characterized by a significant infiltration of classical anti-tumor immune cells, including CD8+ T cells and M1 macrophages, as well as immunosuppressive cells such as Treg cells. Moreover, both autoimmune and immunodeficiency pathways were prominently enriched in the Immune-H subtype. The expression levels of HLA molecules and ICIs were also notably elevated in the Immune-H subtype. These findings suggested that the Immune-H subtype possessed a high degree of

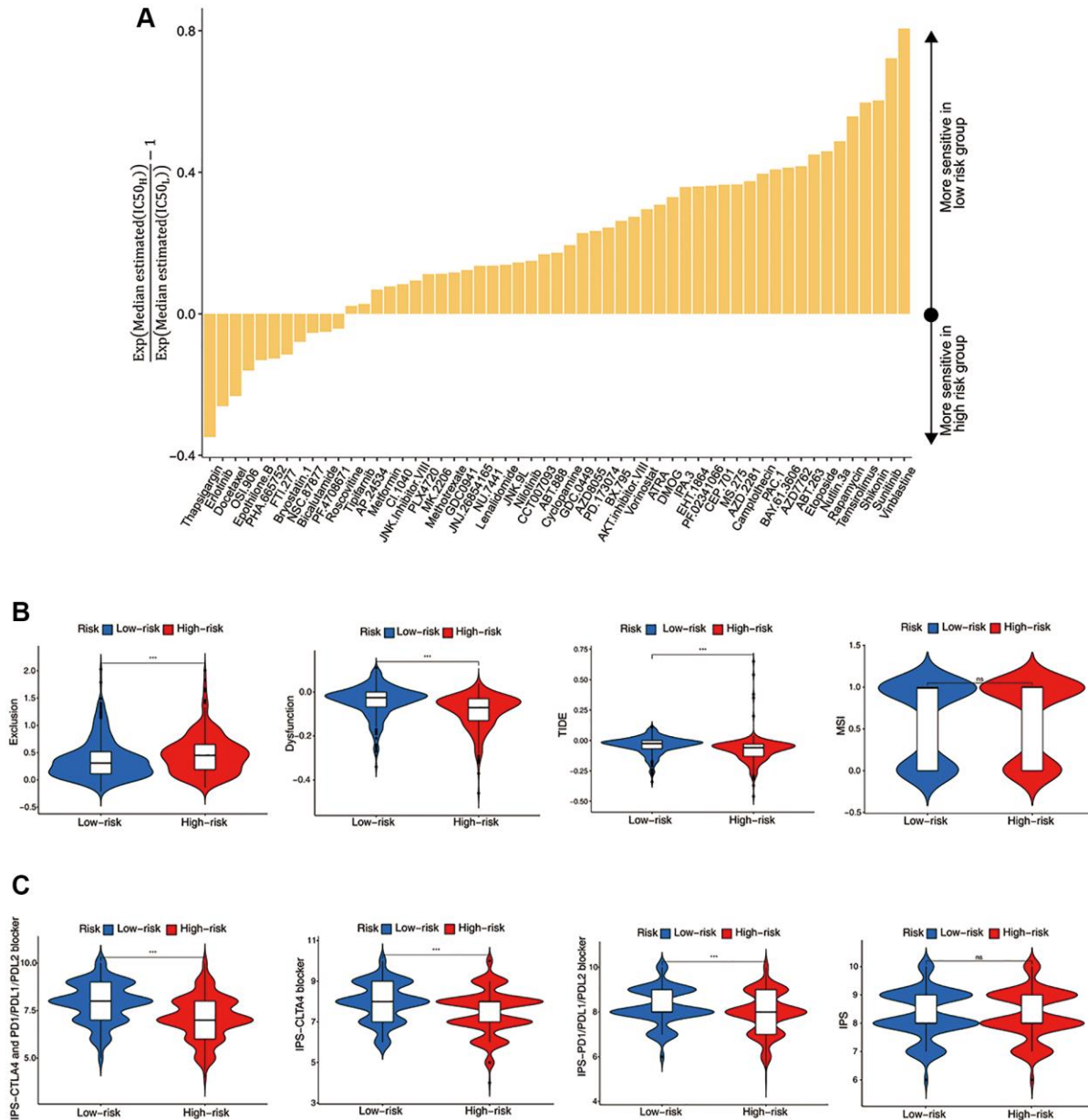


Figure 5. Evaluation of the ICF score in predicting HNSCC treatment responsiveness. (A) The histogram shows the drugs with significant differences of IC50 value between high- and low- risk groups (Wilcoxon test, $p < 0.05$). (B) Comparisons of T cell exclusion and dysfunction scores, the comprehensive TIDE score, and the MSI score between high- and low-risk groups. (C) Comparisons of the IPS values between high- and low-risk groups.

immunogenicity and immune escape potential, similar to that of a “hot” tumor. In contrast, the Immune-L subtype showed a lack of immune cell infiltration and activation of immune-related pathways. This subtype could be considered as a “cold” tumor, where immune cells fail to recognize cancer cells effectively. On the other hand, the Immune-M subtype represented an

intermediate status between “hot” and “cold” tumors, suggesting a mixed immune microenvironment.

Goodman et al. performed a retrospective analysis involving 151 patients with multiple types of solid tumors who were treated with ICIs [21]. Their findings revealed that patients with high TMB (TMB-H)

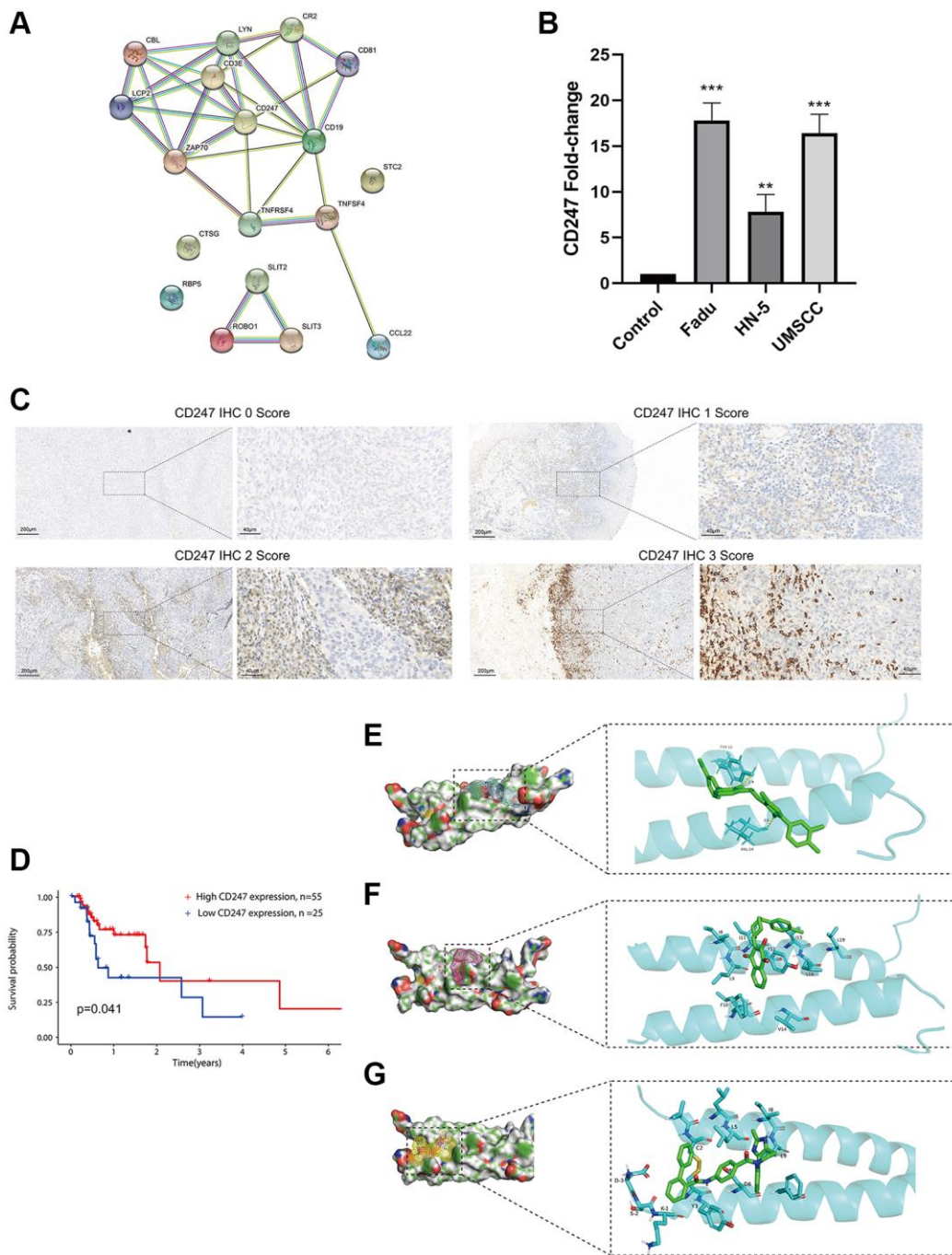


Figure 6. Identification and validation of the key target and prediction of candidate small molecule compounds. (A) The PPI network of the ICF gene signature (interaction score ≥ 0.4). (B) The expression analysis of CD247 in control mucosal epithelia cells and HNSCC cell lines. (C) IHC staining of CD247 in HNSCC tissues. (D) Kaplan-Meier survival analysis of HNSCC patients according to CD247 IHC scores. The molecular docking diagram shows the interaction between the small molecules Eltrombopag (E), ZINC116473771 (F), and Conivaptan (G) with CD247.

exhibited a significantly higher response rate compared to those with low TMB (TMB-L). Several studies have also suggested a positive correlation between TMB-H and improved survival in gastric cancer and ovarian cancer [22, 23]. However, in this study, it was observed that TMB-H was associated with poor survival in patients with HNSCC. Comprehensive analysis suggested that the low-risk group, which mostly comprised patients with TMB-L, may be more favorable for immunotherapy. This group exhibited increased immune cell infiltration, immune checkpoint expression, HLA molecule expression, and higher IPS values, suggesting a stronger immunogenicity. Consequently, the effectiveness of ICIs treatment in HNSCC may be influenced by multiple factors due to the heterogeneity of the tumor microenvironment.

M0 macrophages were typically considered as the precursor cells that can differentiate into M1 or M2 macrophages, but they did not exhibit specific functional properties themselves [24]. In our study, we observed a high infiltration of M0 macrophages in the high-risk group, implying their tumor-promoting role. Recent evidence has also revealed the extensive differentiation and tumorigenic potential of M0 macrophages in hepatocellular carcinoma and glioma, challenging the traditional M1/M2 paradigm [25, 26]. Chan et al. reported that upon contact with cancer cells, active NK cells could transform into a resting state, and played a role in tumorigenesis and metastasis [27]. This was in line with our study, resting NK cells had a higher proportion in the high-risk group. Our results revealed the activation of multiple metabolic reprogramming pathways in the high-risk group, including steroid biosynthesis and the pentose phosphate pathway. Similarly, Ringel et al. demonstrated that tumor cells upregulate the free fatty acid pathway to competitively suppress the fuel utilization and functionality of CD8⁺ T cells, thereby promoting tumor development [28].

In order to identify potential targets for immunotherapy, we focused on the hub gene CD247 of the ICF gene signature. Down-regulation of CD247 has been observed to induce immunosuppression in chronic inflammation and tumors [29]. To explore potential interactions with CD247, we screened over 1300 small molecule compounds approved by the FDA. Eltrombopag, a thrombopoietin receptor agonist that stimulates the proliferation of megakaryocytes [30], may be a candidate small molecule for immunotherapy if it can also act as a TCR agonist to promote anti-tumor immunity. However, further experiments are needed to verify this speculation.

Our study has a few limitations that should be acknowledged. Firstly, the ICF-based classification

strategy requires validation in larger multicenter cohorts. Secondly, due to the absence of expression data from HNSCC patients undergoing immunotherapy, our findings need to be further confirmed in HNSCC patients who have received immunotherapy.

CONCLUSIONS

Based on ICF, we have classified HNSCC into three distinct immunophenotypes (Immune-L, Immune-M and Immune-H), which were associated with different clinical features, molecular profiles, and biological processes. The characteristics of Immune-H were consistent with those of “Hot” tumors, while Immune-L was in line with “Cold” tumors, and Immune-M was intermediate between the two. Furthermore, the ICF score, which was constructed based on the immunophenotypes, demonstrated robust performance in predicting prognosis. The ICF score was also found to be associated with TMB, immune checkpoints, HLA alleles, and responsiveness to chemotherapy and immunotherapy. Collectively, our work provides a new perspective on the immune microenvironment of HNSCC, which facilitates the interpretation of the HNSCC heterogeneity and developing personalized/precision medicine.

Abbreviations

ICF: immune cell function; HNSCC: head and neck squamous cell carcinoma; WGCNA: weighted gene co-expression network analysis; GSVA: gene set variation analysis; ICI: immune checkpoint inhibitor; PD-L1: programmed death ligand-1; TME: tumor microenvironment; GSEA: gene set enrichment analysis; PPI: protein-protein interaction; DEG: differentially expressed gene; IRDEG: immune-related differentially expressed gene; PIG: prognosis-related immune gene; TF: transcription factor; TMB: tumor mutation burden; IPS: immunophenoscore; GPI-AP: glycosylphosphatidylinositol-anchored protein.

AUTHOR CONTRIBUTIONS

W.-W.L.: writing-investigation, original draft preparation; L.-D.P.: writing-review and editing, funding acquisition; L.-W.M., W.-D.M. Z.-Z.Y. and Q.Y.: methodology, software; X.-J.N. and C.-S.D.: data curation, resources. All authors have read and agreed to the published version of the manuscript.

ACKNOWLEDGMENTS

We would like to exert compelling appreciation for the TCGA and GSE65858 projects.

CONFLICTS OF INTEREST

The authors declare that the research was conducted in the absence of any commercial or financial relationships that could be construed as a potential conflict of interest.

ETHICAL STATEMENT AND CONSENT

The study was conducted in accordance with the principles outlined in the Declaration of Helsinki and was approved by the Ethics Committee of Qilu Hospital of Shandong University (KYLL-2020(KS)-320). All patients enrolled from our institution provided written informed consent.

FUNDING

This research was supported by the National Natural Science Foundation of China (82071918 to Dapeng Lei) and Natural Science Foundation of Shandong Province (ZR2023QH515 to Wenlun Wang).

REFERENCES

1. Chow LQM. Head and Neck Cancer. *N Engl J Med*. 2020; 382:60–72.
<https://doi.org/10.1056/NEJMra1715715>
PMID:[31893516](https://pubmed.ncbi.nlm.nih.gov/31893516/)
2. Sung H, Ferlay J, Siegel RL, Laversanne M, Soerjomataram I, Jemal A, Bray F. Global Cancer Statistics 2020: GLOBOCAN Estimates of Incidence and Mortality Worldwide for 36 Cancers in 185 Countries. *CA Cancer J Clin*. 2021; 71:209–49.
<https://doi.org/10.3322/caac.21660>
PMID:[33538338](https://pubmed.ncbi.nlm.nih.gov/33538338/)
3. Carlisle JW, Steuer CE, Owonikoko TK, Saba NF. An update on the immune landscape in lung and head and neck cancers. *CA Cancer J Clin*. 2020; 70:505–17.
<https://doi.org/10.3322/caac.21630>
PMID:[32841388](https://pubmed.ncbi.nlm.nih.gov/32841388/)
4. Ferris RL, Blumenschein G Jr, Fayette J, Guigay J, Colevas AD, Licitra L, Harrington K, Kasper S, Vokes EE, Even C, Worden F, Saba NF, Iglesias Docampo LC, et al. Nivolumab for Recurrent Squamous-Cell Carcinoma of the Head and Neck. *N Engl J Med*. 2016; 375:1856–67.
<https://doi.org/10.1056/NEJMoa1602252>
PMID:[27718784](https://pubmed.ncbi.nlm.nih.gov/27718784/)
5. Mehra R, Seiwert TY, Gupta S, Weiss J, Gluck I, Eder JP, Burtness B, Tahara M, Keam B, Kang H, Muro K, Geva R, Chung HC, et al. Efficacy and safety of pembrolizumab in recurrent/metastatic head and neck squamous cell carcinoma: pooled analyses after long-term follow-up in KEYNOTE-012. *Br J Cancer*. 2018; 119:153–9.
<https://doi.org/10.1038/s41416-018-0131-9>
PMID:[29955135](https://pubmed.ncbi.nlm.nih.gov/29955135/)
6. Cohen EEW, Bell RB, Bifulco CB, Burtness B, Gillison ML, Harrington KJ, Le QT, Lee NY, Leidner R, Lewis RL, Licitra L, Mehanna H, Mell LK, et al. The Society for Immunotherapy of Cancer consensus statement on immunotherapy for the treatment of squamous cell carcinoma of the head and neck (HNSCC). *J Immunother Cancer*. 2019; 7:184.
<https://doi.org/10.1186/s40425-019-0662-5>
PMID:[31307547](https://pubmed.ncbi.nlm.nih.gov/31307547/)
7. Bagaev A, Kotlov N, Nomie K, Svekolkin V, Gafurov A, Isaeva O, Osokin N, Kozlov I, Frenkel F, Gancharova O, Almog N, Tsiper M, Ataulkhanov R, Fowler N. Conserved pan-cancer microenvironment subtypes predict response to immunotherapy. *Cancer Cell*. 2021; 39:845–65.e7.
<https://doi.org/10.1016/j.ccell.2021.04.014>
PMID:[34019806](https://pubmed.ncbi.nlm.nih.gov/34019806/)
8. Baysal H, Siozopoulou V, Zaryouh H, Hermans C, Lau HW, Lambrechts H, Fransen E, De Pauw I, Jacobs J, Peeters M, Pauwels P, Vermorken JB, Smits E, et al. The prognostic impact of the immune signature in head and neck squamous cell carcinoma. *Front Immunol*. 2022; 13:1001161.
<https://doi.org/10.3389/fimmu.2022.1001161>
PMID:[36268020](https://pubmed.ncbi.nlm.nih.gov/36268020/)
9. Lou X, Gao H, Xu X, Ye Z, Zhang W, Wang F, Chen J, Zhang Y, Chen X, Qin Y, Yu X, Ji S. The Interplay of Four Main Pathways Recomposes Immune Landscape in Primary and Metastatic Gastroenteropancreatic Neuroendocrine Tumors. *Front Oncol*. 2022; 12:808448.
<https://doi.org/10.3389/fonc.2022.808448>
PMID:[35664743](https://pubmed.ncbi.nlm.nih.gov/35664743/)
10. Poźniak J, Nsengimana J, Laye JP, O'Shea SJ, Diaz JMS, Droop AP, Folia A, Harland M, Davies JR, Mell T, Randerson-Moor JA, Muralidhar S, Hogan SA, et al. Genetic and Environmental Determinants of Immune Response to Cutaneous Melanoma. *Cancer Res*. 2019; 79:2684–96.
<https://doi.org/10.1158/0008-5472.CAN-18-2864>
PMID:[30773503](https://pubmed.ncbi.nlm.nih.gov/30773503/)
11. Chen DS, Mellman I. Elements of cancer immunity and the cancer-immune set point. *Nature*. 2017; 541:321–30.
<https://doi.org/10.1038/nature21349>
PMID:[28102259](https://pubmed.ncbi.nlm.nih.gov/28102259/)
12. Thorsson V, Gibbs DL, Brown SD, Wolf D, Bortone DS, Ou Yang TH, Porta-Pardo E, Gao GF, Plaisier CL, Eddy JA, Ziv E, Culhane AC, Paull EO, et al, and Cancer Genome Atlas Research Network. The Immune

- Landscape of Cancer. Immunity. 2018; 48:812–30.e14.
<https://doi.org/10.1016/j.immuni.2018.03.023>
PMID:[29628290](https://pubmed.ncbi.nlm.nih.gov/29628290/)
13. He Y, Jiang Z, Chen C, Wang X. Classification of triple-negative breast cancers based on Immunogenomic profiling. *J Exp Clin Cancer Res*. 2018; 37:327.
<https://doi.org/10.1186/s13046-018-1002-1>
PMID:[30594216](https://pubmed.ncbi.nlm.nih.gov/30594216/)
14. Prasetyanti PR, Medema JP. Intra-tumor heterogeneity from a cancer stem cell perspective. *Mol Cancer*. 2017; 16:41.
<https://doi.org/10.1186/s12943-017-0600-4>
PMID:[28209166](https://pubmed.ncbi.nlm.nih.gov/28209166/)
15. Geeleher P, Cox NJ, Huang RS. Clinical drug response can be predicted using baseline gene expression levels and in vitro drug sensitivity in cell lines. *Genome Biol*. 2014; 15:R47.
<https://doi.org/10.1186/gb-2014-15-3-r47>
PMID:[24580837](https://pubmed.ncbi.nlm.nih.gov/24580837/)
16. Jiang P, Gu S, Pan D, Fu J, Sahu A, Hu X, Li Z, Traugh N, Bu X, Li B, Liu J, Freeman GJ, Brown MA, et al. Signatures of T cell dysfunction and exclusion predict cancer immunotherapy response. *Nat Med*. 2018; 24:1550–8.
<https://doi.org/10.1038/s41591-018-0136-1>
PMID:[30127393](https://pubmed.ncbi.nlm.nih.gov/30127393/)
17. Charoentong P, Finotello F, Angelova M, Mayer C, Efremova M, Rieder D, Hackl H, Trajanoski Z. Pan-cancer Immunogenomic Analyses Reveal Genotype-Immuno-phenotype Relationships and Predictors of Response to Checkpoint Blockade. *Cell Rep*. 2017; 18:248–62.
<https://doi.org/10.1016/j.celrep.2016.12.019>
PMID:[28052254](https://pubmed.ncbi.nlm.nih.gov/28052254/)
18. Zhai E, Liang W, Lin Y, Huang L, He X, Cai S, Chen J, Zhang N, Li J, Zhang Q, He Y, Zeng Z, Chen M, et al. HSP70/HSP90-Organizing Protein Contributes to Gastric Cancer Progression in an Autocrine Fashion and Predicts Poor Survival in Gastric Cancer. *Cell Physiol Biochem*. 2018; 47:879–92.
<https://doi.org/10.1159/000490080>
PMID:[29843139](https://pubmed.ncbi.nlm.nih.gov/29843139/)
19. Du K, Zou J, Wang B, Liu C, Khan M, Xie T, Huang X, Shen P, Tian Y, Yuan Y. A Metabolism-Related Gene Prognostic Index Bridging Metabolic Signatures and Antitumor Immune Cycling in Head and Neck Squamous Cell Carcinoma. *Front Immunol*. 2022; 13:857934.
<https://doi.org/10.3389/fimmu.2022.857934>
PMID:[35844514](https://pubmed.ncbi.nlm.nih.gov/35844514/)
20. Zhang X, Shi M, Chen T, Zhang B. Characterization of the Immune Cell Infiltration Landscape in Head and Neck Squamous Cell Carcinoma to Aid Immunotherapy. *Mol Ther Nucleic Acids*. 2020; 22:298–309.
<https://doi.org/10.1016/j.omtn.2020.08.030>
PMID:[33230435](https://pubmed.ncbi.nlm.nih.gov/33230435/)
21. Goodman AM, Kato S, Bazhenova L, Patel SP, Frampton GM, Miller V, Stephens PJ, Daniels GA, Kurzrock R. Tumor Mutational Burden as an Independent Predictor of Response to Immunotherapy in Diverse Cancers. *Mol Cancer Ther*. 2017; 16:2598–608.
<https://doi.org/10.1158/1535-7163.MCT-17-0386>
PMID:[28835386](https://pubmed.ncbi.nlm.nih.gov/28835386/)
22. Li C, Pan J, Jiang Y, Yu Y, Jin Z, Chen X. Characteristics of the Immune Cell Infiltration Landscape in Gastric Cancer to Assistant Immunotherapy. *Front Genet*. 2022; 12:793628.
<https://doi.org/10.3389/fgene.2021.793628>
PMID:[35069691](https://pubmed.ncbi.nlm.nih.gov/35069691/)
23. Liu J, Wang Y, Yuan S, Wei J, Bai J. Construction of an Immune Cell Infiltration Score to Evaluate the Prognosis and Therapeutic Efficacy of Ovarian Cancer Patients. *Front Immunol*. 2021; 12:751594.
<https://doi.org/10.3389/fimmu.2021.751594>
PMID:[34745124](https://pubmed.ncbi.nlm.nih.gov/34745124/)
24. Shapouri-Moghaddam A, Mohammadian S, Vazini H, Taghadosi M, Esmaeili SA, Mardani F, Seifi B, Mohammadi A, Afshari JT, Sahebkar A. Macrophage plasticity, polarization, and function in health and disease. *J Cell Physiol*. 2018; 233:6425–40.
<https://doi.org/10.1002/jcp.26429>
PMID:[29319160](https://pubmed.ncbi.nlm.nih.gov/29319160/)
25. Zhang Y, Zou J, Chen R. An M0 macrophage-related prognostic model for hepatocellular carcinoma. *BMC Cancer*. 2022; 22:791.
<https://doi.org/10.1186/s12885-022-09872-y>
PMID:[35854246](https://pubmed.ncbi.nlm.nih.gov/35854246/)
26. Huang L, Wang Z, Chang Y, Wang K, Kang X, Huang R, Zhang Y, Chen J, Zeng F, Wu F, Zhao Z, Li G, Huang H, et al. *EFEMP2* indicates assembly of M0 macrophage and more malignant phenotypes of glioma. *Aging (Albany NY)*. 2020; 12:8397–412.
<https://doi.org/10.18632/aging.103147>
PMID:[32396873](https://pubmed.ncbi.nlm.nih.gov/32396873/)
27. Chan IS, Knútsdóttir H, Ramakrishnan G, Padmanaban V, Warriar M, Ramirez JC, Dunworth M, Zhang H, Jaffee EM, Bader JS, Ewald AJ. Cancer cells educate natural killer cells to a metastasis-promoting cell state. *J Cell Biol*. 2020; 219:e202001134.
<https://doi.org/10.1083/jcb.202001134>
PMID:[32645139](https://pubmed.ncbi.nlm.nih.gov/32645139/)
28. Ringel AE, Drijvers JM, Baker GJ, Catozzi A, García-

Cañaveras JC, Gassaway BM, Miller BC, Juneja VR, Nguyen TH, Joshi S, Yao CH, Yoon H, Sage PT, et al. Obesity Shapes Metabolism in the Tumor Microenvironment to Suppress Anti-Tumor Immunity. *Cell*. 2020; 183:1848–66.e26.

<https://doi.org/10.1016/j.cell.2020.11.009>

PMID:[33301708](https://pubmed.ncbi.nlm.nih.gov/33301708/)

29. Baniyash M. TCR zeta-chain downregulation: curtailing an excessive inflammatory immune response. *Nat Rev Immunol*. 2004; 4:675–87.

<https://doi.org/10.1038/nri1434>

PMID:[15343367](https://pubmed.ncbi.nlm.nih.gov/15343367/)

30. Fattizzo B, Levati G, Cassin R, Barcellini W. Eltrombopag in Immune Thrombocytopenia, Aplastic Anemia, and Myelodysplastic Syndrome: From Megakaryopoiesis to Immunomodulation. *Drugs*. 2019; 79:1305–19.

<https://doi.org/10.1007/s40265-019-01159-0>

PMID:[31292909](https://pubmed.ncbi.nlm.nih.gov/31292909/)

SUPPLEMENTARY MATERIALS

Supplementary Results

Impact of immune cell infiltration on patient survival

Survival analysis was performed to assess the impact of immune cell infiltration on patient outcomes (Supplementary Figure 2). The results revealed that patients with higher levels of infiltration of naive B cells, resting dendritic cells, resting mast cells, plasma cells, helper follicular T cells, and Treg cells had more favorable prognoses. These immune cell types were predominantly abundant in the Immune-H subtype. On the other hand, patients with higher levels of activated mast cells, neutrophils, resting CD4+ memory cells, and M2 macrophages had poorer prognoses.

Identification of the immunophenotype-related gene module and hub gene

WGCNA analysis identified 16 gene modules potentially responsible for the immunophenotype (Supplementary Figure 4A). The black module consisted of 1907 genes (Supplementary Table 8) that exhibited a positive correlation with the Immune-H subtype and a negative correlation with the Immune-L subtype (Supplementary Figure 4B). Moreover, the black module gene showed a significant association with survival time. GO and KEGG analyses indicated that black module genes were significantly enriched in pathways related to immune cell communication (Supplementary Figure 4C, 4D). A protein-protein interaction (PPI) network was constructed, consisting of 154 hub genes from the black module (Supplementary Figure 4E). Within this network, SAHS3, CD53, and NCKAP1L occupied central positions. Additionally, SASH3, CD53, and NCKAP1L showed higher expression levels in the Immune-H subtype, while lower expression levels in the Immune-L subtype (Supplementary Figure 4F). These genes might possess the strongest biological significance within the black module.

Exploration of transcription factors in the regulation of prognosis-related immune genes (PIGs)

We also investigated the involvement of transcription factors in the regulation of PIGs through co-expression analysis (Supplementary Figure 6A). Our analysis revealed fifteen transcription factors, including FOXP3, IRF1, and STAT4, which exhibited redundancy in the regulation of PIGs. These transcription factors may play crucial roles in driving different risk groups. Additionally, the PPI network displayed potential interactions between PIGs and the identified transcription

factors. Notably, CTLA4, CD3D, and CD19 were found to be positioned at the core of the network (Supplementary Figure 6B).

Synergistic effect of the ICF Score and TMB on prognosis

Survival analysis revealed that patients with TMB-H had significantly worse survival compared to those with TMB-L (Supplementary Figure 8A). Furthermore, the combination of the ICF score and TMB had a synergistic effect in predicting prognosis. Patients with both TMB-H and high-risk scores had the shortest median survival time, while those with TMB-L and low-risk scores had the most favorable survival outcome (Supplementary Figure 8B).

Correlation between ICF signature genes and infiltration of immune cells

We investigated the correlation between the expression levels of the ICF signature genes and the infiltration of immune cells (Supplementary Figure 9). The majority of the signature genes displayed significant correlations with immune cell infiltration. Notably, ZAP70 exhibited a positive correlation with CD8+ T cells and follicular helper T cells, while showing a negative correlation with activated mast cells and M0 macrophages. Besides, CD19 demonstrated a positive correlation with plasma cells and naive B cells, but a negative correlation with M0 macrophages.

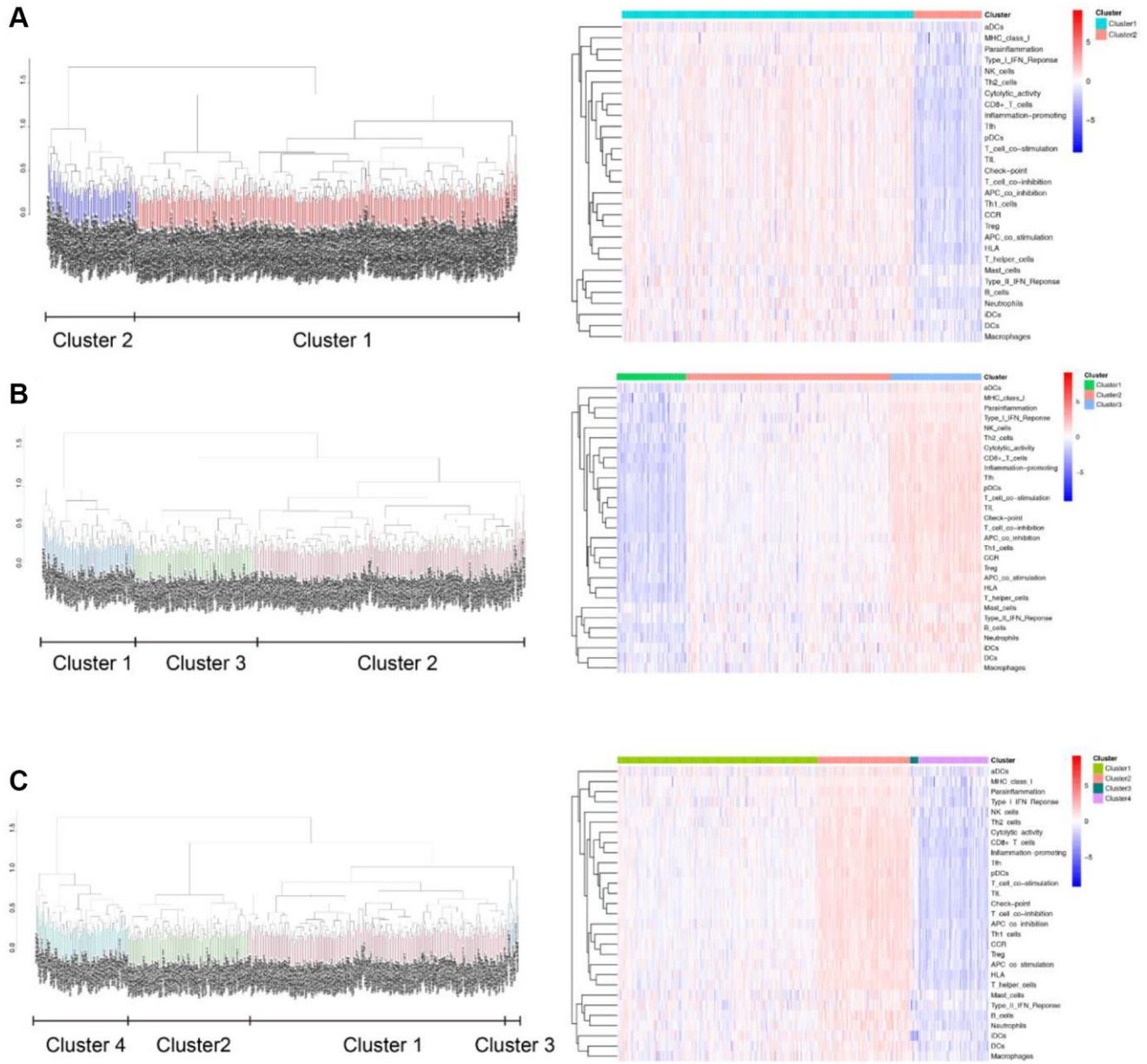
Advantages of ICF immunophenotyping strategy in HNSCC classification

We further compared our ICF immunophenotyping strategy with a previously reported immune typing strategy by Ve´steinn et al. In their study, solid tumors were categorized into six immune subtypes, with HNSCC primarily classified as C1 (wound healing) and C2 (INF- γ dominant) [1]. However, this classification system heavily relied on the differentiation of CD4+ T cells, which may not effectively distinguish HNSCC (Supplementary Figure 10). In contrast, our method divided HNSCC into three ICF subtypes and further stratified them into high- and low-risk groups. The Immune-H subtype predominantly fell into the low-risk group, while the Immune-L subtype mainly belonged to the high-risk group. Additionally, the low-risk group showed a higher proportion of patients with improved survival outcomes. As a result, our ICF-guided immunophenotyping strategy demonstrated clear advantages in characterizing HNSCC.

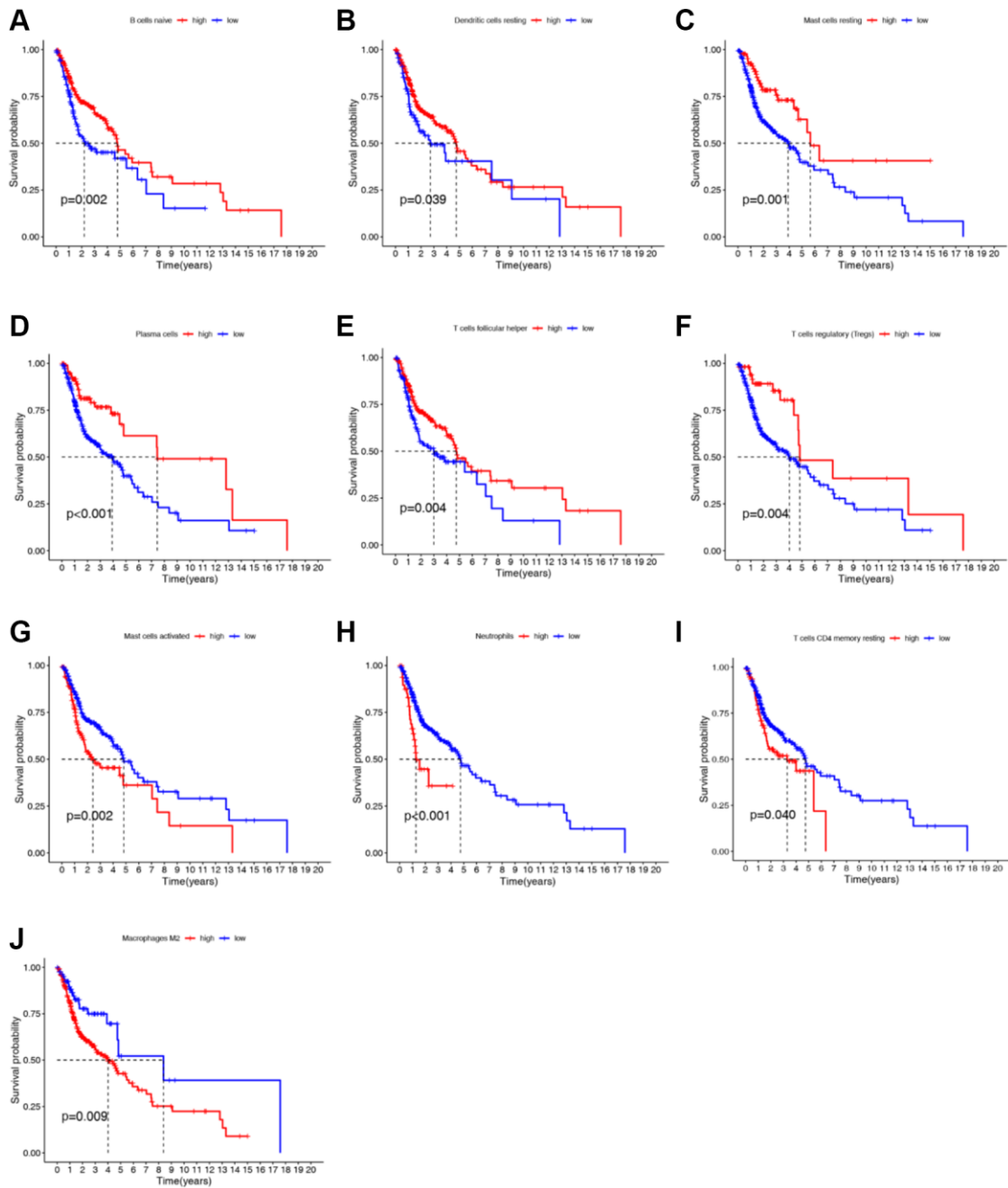
Supplementary References

1. Thorsson V, Gibbs DL, Brown SD, Wolf D, Bortone DS, Ou Yang TH, Porta-Pardo E, Gao GF, Plaisier CL, Eddy JA, Ziv E, Culhane AC, Paull EO, and Cancer Genome Atlas Research Network. The Immune Landscape of Cancer. *Immunity*. 2018; 48:812–30.e14.
<https://doi.org/10.1016/j.immuni.2018.03.023>
PMID:[29628290](https://pubmed.ncbi.nlm.nih.gov/29628290/)

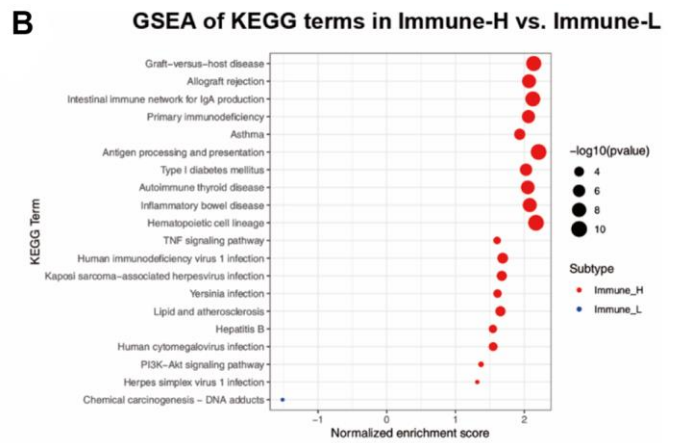
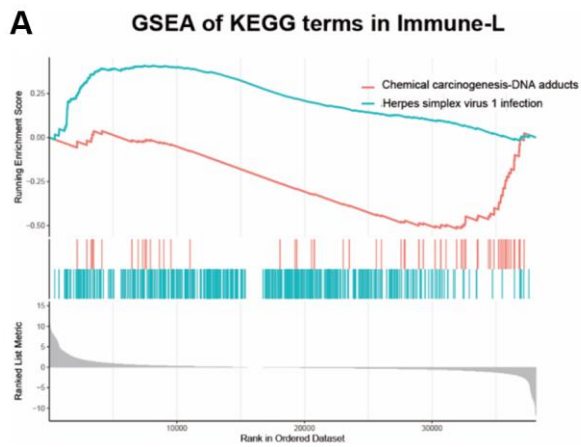
Supplementary Figures



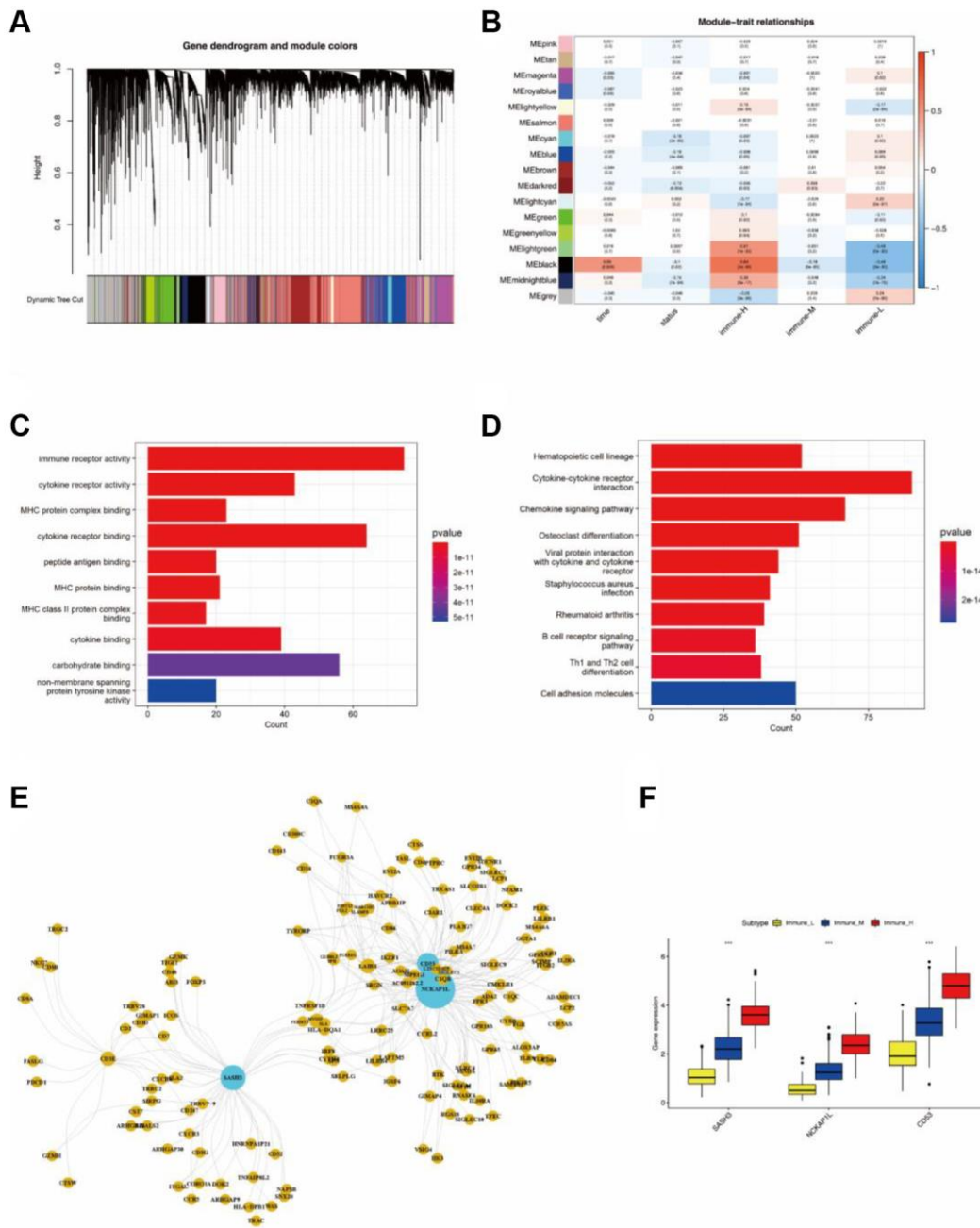
Supplementary Figure 1. Cluster dendrogram (left panel) and the enrichment analysis of 29 functional immune cells (right panel) when TCGA-HNSCC samples were divided into 2 (A), 3 (B) and 4 (C) clusters.



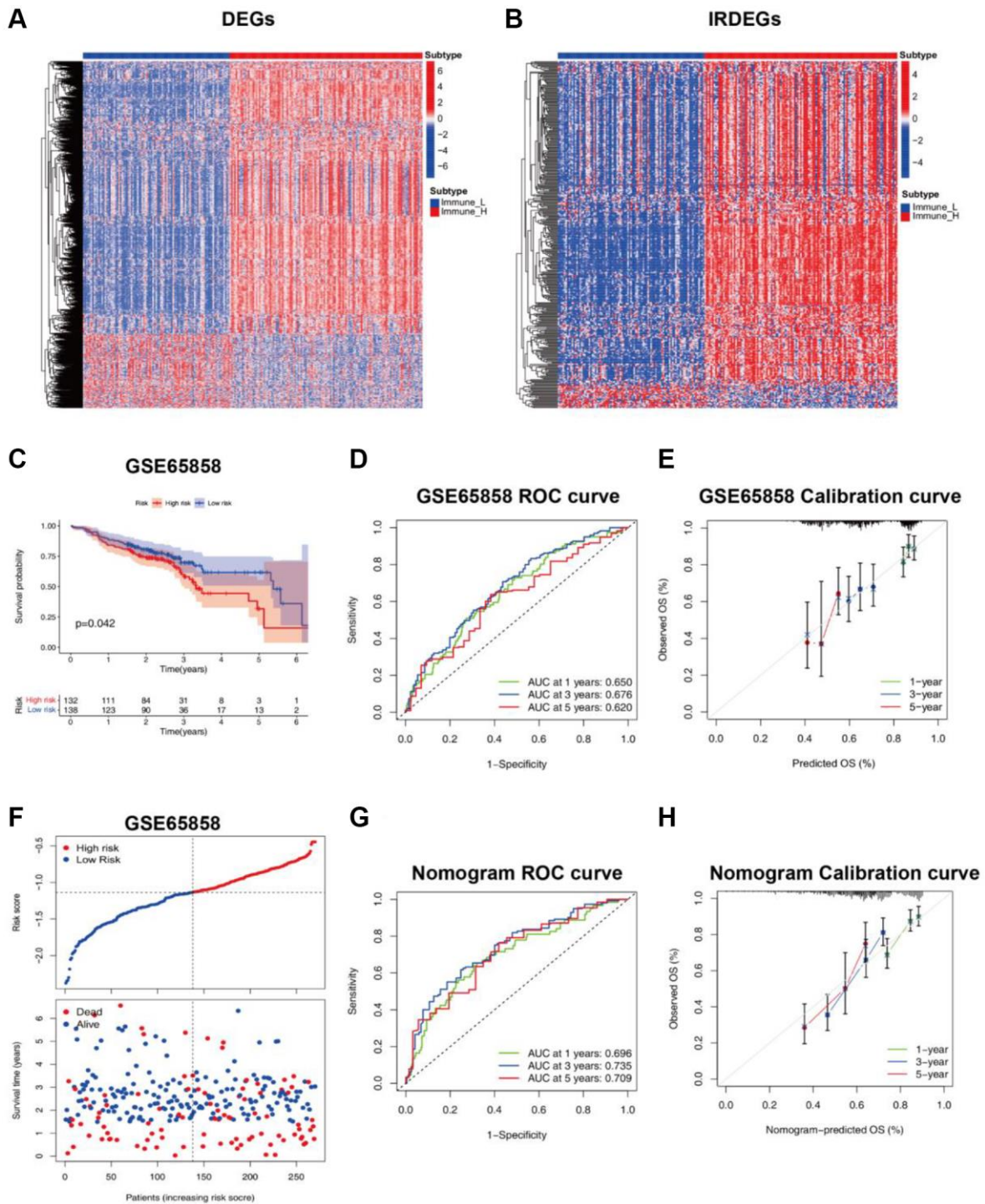
Supplementary Figure 2. Survival analyses based on immune cell infiltration. (A) Naïve B cells, (B) resting dendritic cells, (C) resting mast cells, (D) plasma cells, (E) T follicular helper cells, (F) regulator T cells, (G) activated mast cells, (H) neutrophils, (I) memory resting CD4+ T cells, and (J) M2 macrophages.



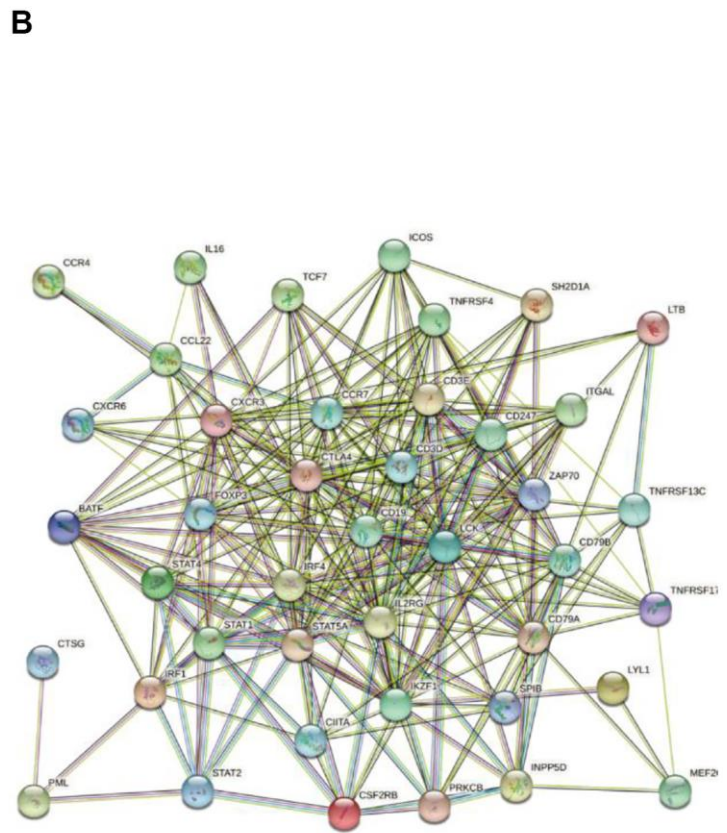
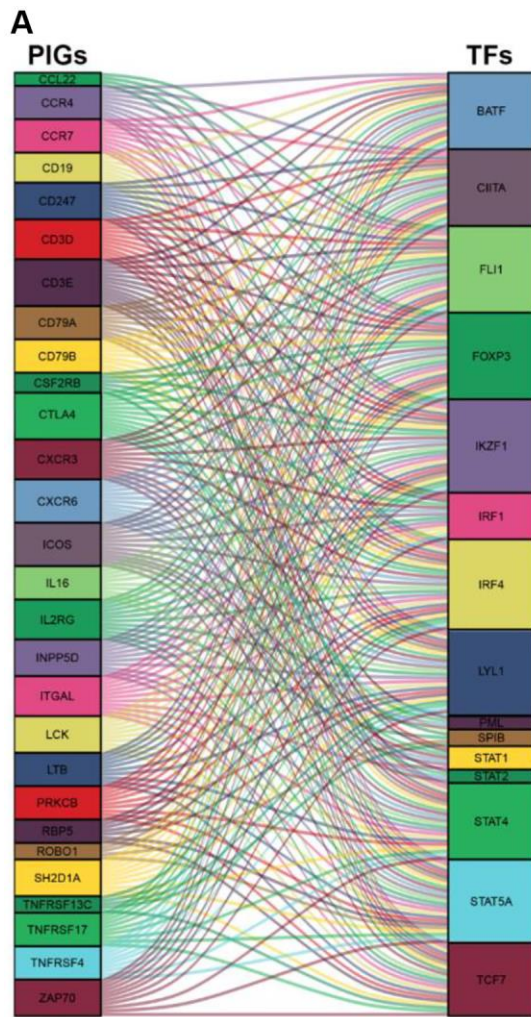
Supplementary Figure 3 Biological processes in different immunophenotypes. (A) GSEA shows only the chemical carcinogenesis (DNA adducts) pathway is enriched in the Immune-L subtype. (B) The bubble plot shows the enrichment result of KEGG terms in Immune-H and Immune-L subtypes.



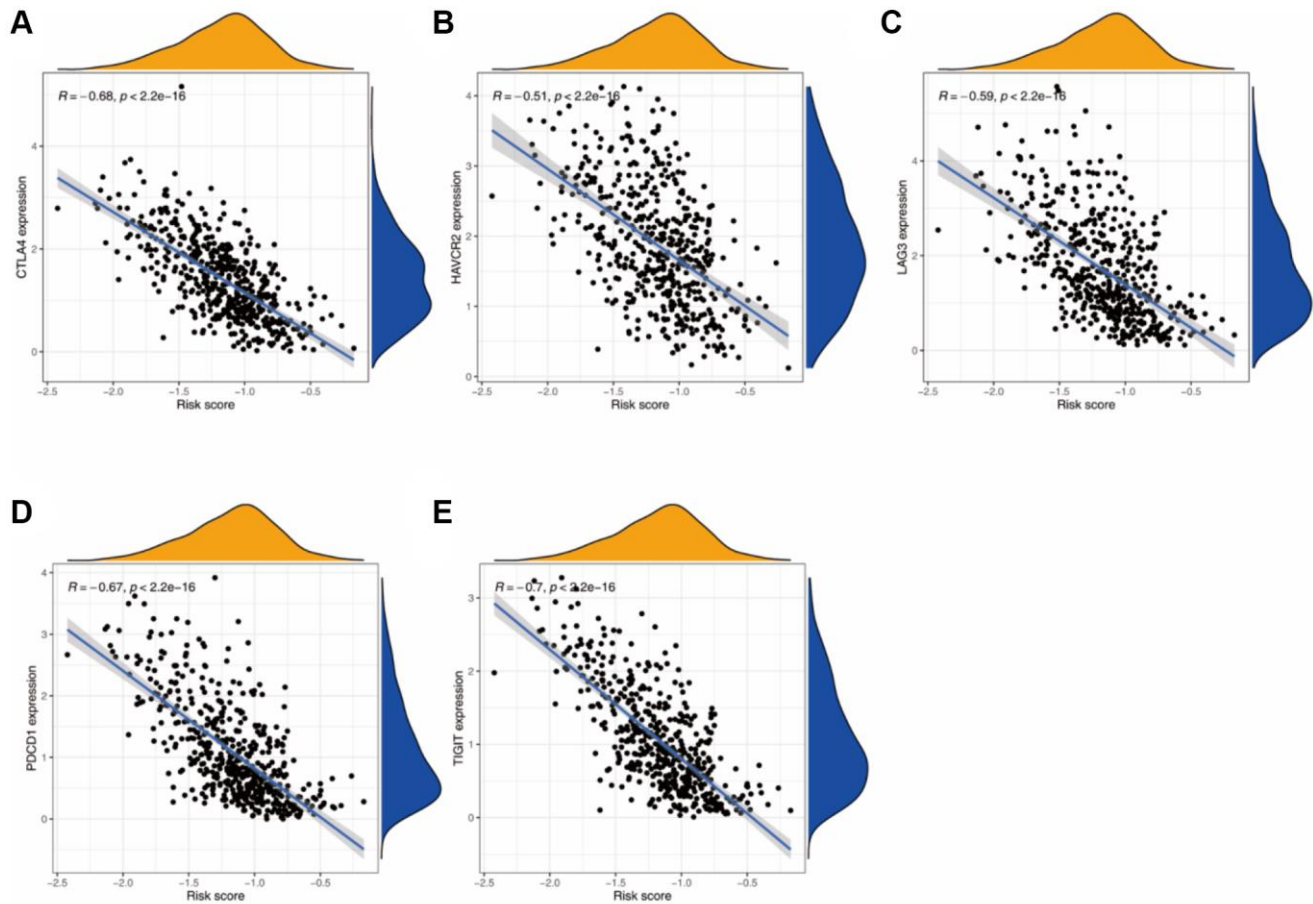
Supplementary Figure 4. Identification of the immunophenotype-related gene module by WGCNA. (A) Cluster dendrogram of gene co-expression modules after merged (1-TOM). **(B)** Correlation analysis of gene modules and phenotypes of HNSCC. GO functional enrichment **(C)** and KEGG pathway enrichment **(D)** analyses for genes in the black module of WGCNA. **(E)** The protein-protein interaction network of the hub genes in the black module. **(F)** The expression levels of SAHS3, CD53 and NCKAP1L in the three immunophenotypes.



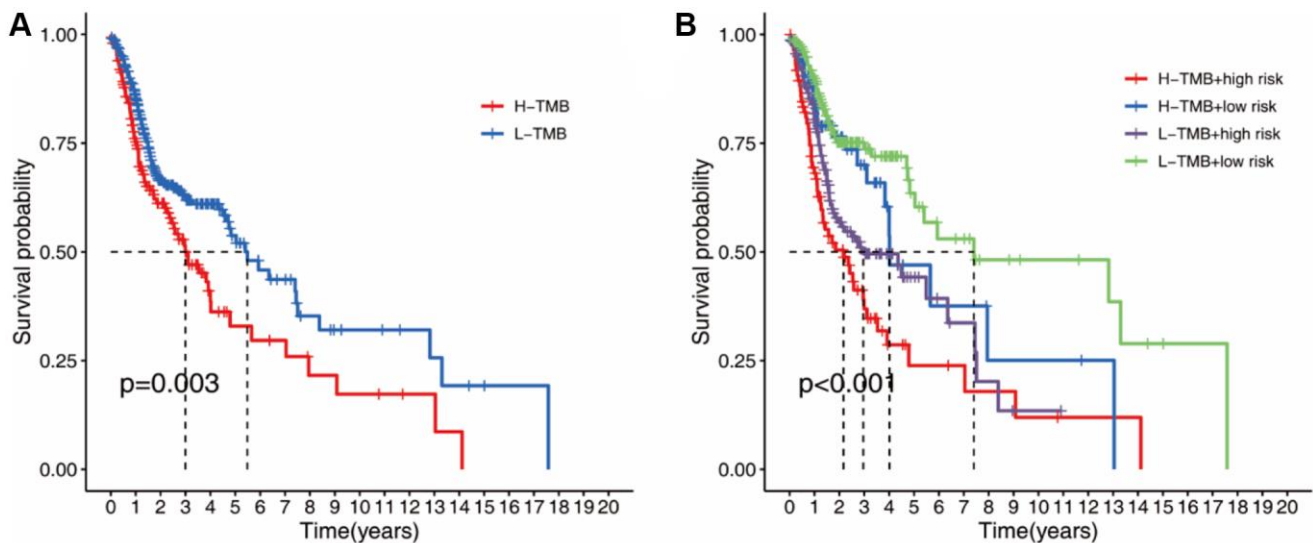
Supplementary Figure 5. Construction and validation of the ICF gene signature. Heatmap of DEGs (A) and IRDEGs (B) between the Immune-H and Immune-L subtypes. (C) Comparisons of overall survival between high- and low-risk groups in the test set. The ROC curve (D) and calibration curve (E) of the ICF score for predicting 1-year, 3-year and 5-year survival in the test set. (F) Correspondence between risk scores and survival in the test set. The ROC curve (G) and calibration curve (H) of the nomogram for predicting overall survival at 1-year, 3-year and 5-year.



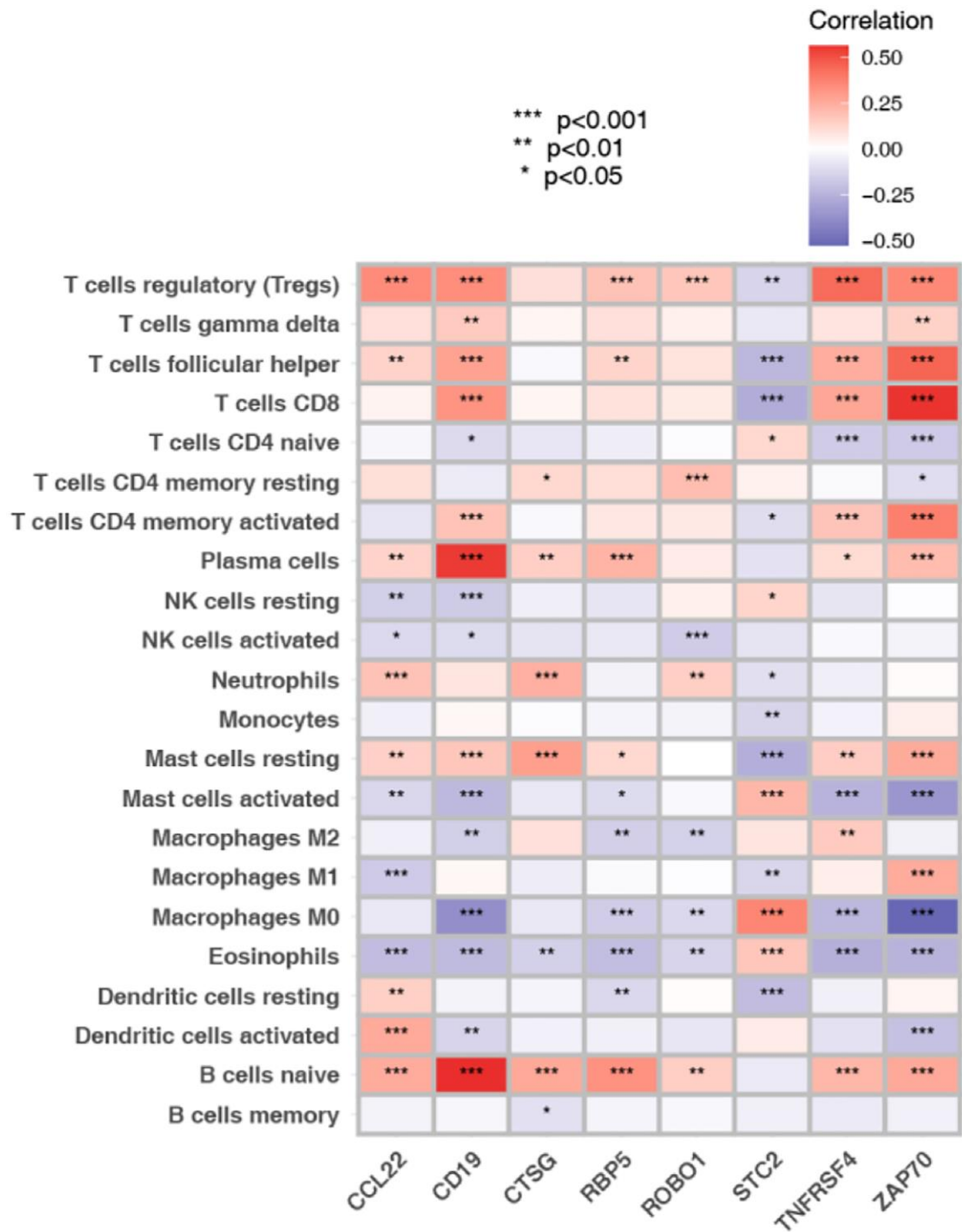
Supplementary Figure 6. Analysis of candidate transcription factors (TFs) for prognosis-related immune genes (PIGs). (A) The alluvial diagram shows the TFs co-expressed with PIGs, and the lines indicate the co-expressed relationship between the two. **(B)** Protein-protein interaction network of PIGs and TFs.



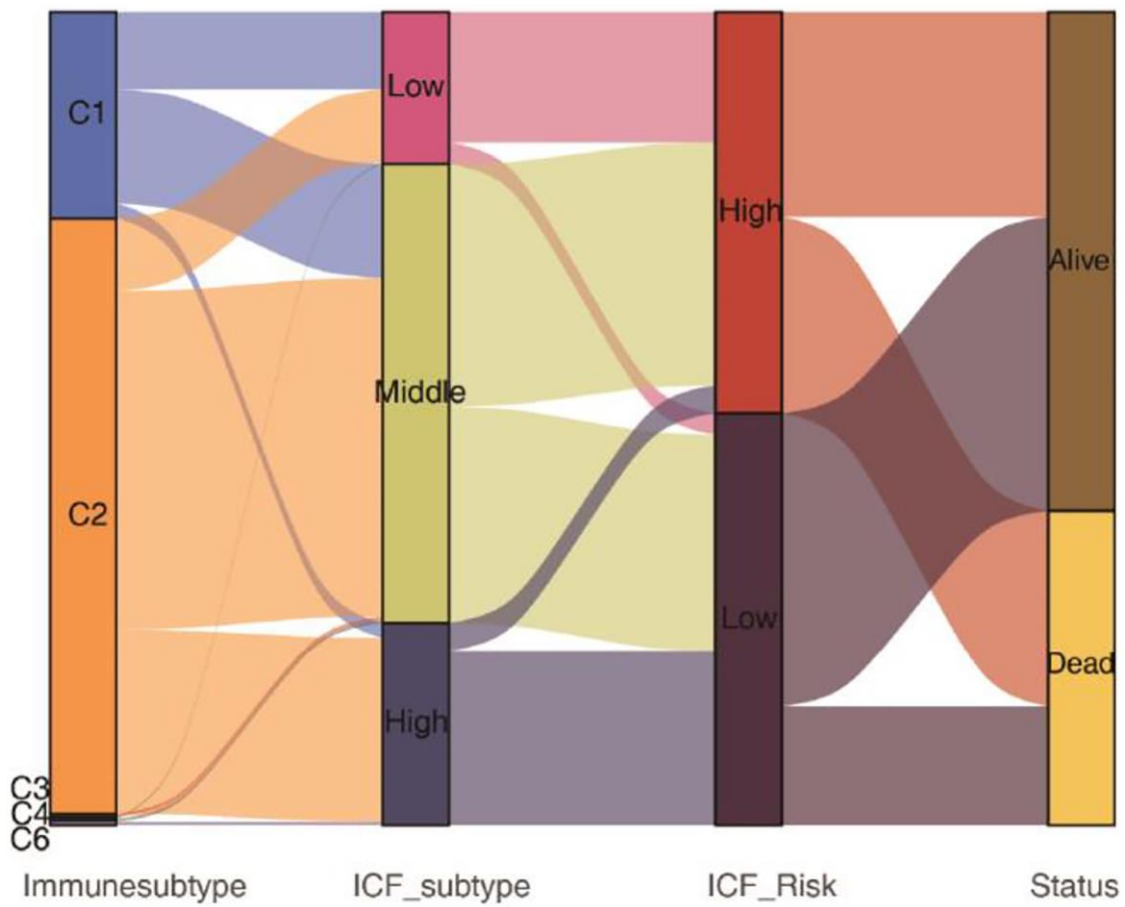
Supplementary Figure 7. The correlations between immune checkpoints and ICF scores in HNSCC. CTLA4 (A), HAVCR2 (B), LAG3 (C), PDCD1 (D), and TIGIT (E).



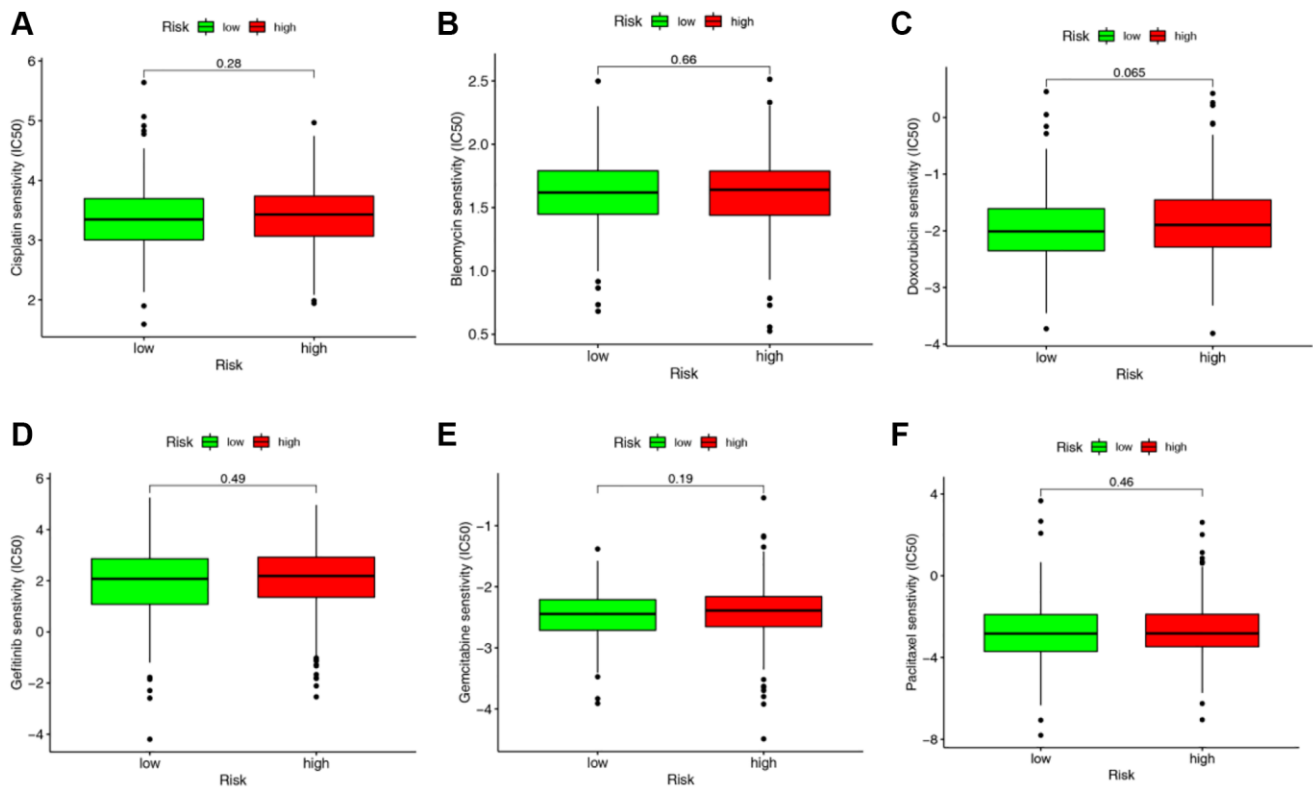
Supplementary Figure 8. Survival analysis for HNSCC patients stratified by TMB and ICF risk score. (A) Kaplan-Meier survival analysis for HNSCC patients with different TMB. (B) Kaplan-Meier survival analysis for patients according to TMB and ICF score stratifications.



Supplementary Figure 9. Correlation analyses between the model genes and immune infiltrating cells.



Supplementary Figure 10. The alluvial diagram shows the correspondence of pan-cancer immune subtypes, ICF subtypes, ICF risk groups and the survival status in HNSCC.



Supplementary Figure 11. Comparisons of the IC50 values of common HNSCC drugs between high-risk and low-risk groups. Cisplatin (A), Bleomycin (B), Doxorubicin (C), Gefitinib (D), Gemcitabine (E), Paclitaxel (F).

Supplementary Tables

Please browse Full Text version to see the data of Supplementary Tables 1, 3, 5 and 8.

Supplementary Table 1. 29 immune gene signatures (gene sets).

Supplementary Table 2. qRT-PCR primer sequences.

CCL2	Forward	GATCTCAGTGCAGAGGCTCG
	Reverse	TCTCCTTGGCCACAATGGTC
CD19	Forward	CTCCCATACCTCCCTGGTCA
	Reverse	GCCCATGACCCACATCTCTC
CTSG	Forward	GAGTCAGACGGAATCGAAACG
	Reverse	CGGAGTGTATCTGTTCCCCTC
RBP5	Forward	CTGGCGTCCCAAATGAAAGA
	Reverse	GAGAGCGGAGATTGGTTGTTCT
ROBO1	Forward	TCCACACAGCAATAGCGAAG
	Reverse	CCTGTAACATGGGCTGGAGT
STC2	Forward	ATGCTACCTCAAGCACGACC
	Reverse	TCTGCTCACACTGAACC
TNFSFR4	Forward	ATGGAAGGGGAAGGGGTTCAACC
	Reverse	TCACAGTGGTACTTGGTTCACAG
ZAP70	Forward	GTTGACTCATCCTCAGAGACGAAT
	Reverse	AGGTTATCGCGCTTCAGGAA
CD247	Forward	GGCACAGTTGCCGATTACAGA
	Reverse	CTGCTGAACTTCACTCTCAGG

Supplementary Table 3. ssGSEA analysis of 29 immune gene signatures in HNSCC samples.

Supplementary Table 4. Clinicopathological features of the training set and the test set.

Total	train set (TCGA-HNSC)	test set (GSE65858)	<i>P</i> -value (Chi-Square Test)
	499	270	
Age			
≤65	324	86	<0.001
>65	175	184	
Gender			
Female	133	47	0.004
Male	366	223	
T stage			
T0-1	46	35	0.728
T2	131	80	
T3	96	58	
T4	171	97	
Unknown	55	0	

N stage					
N0	170	94			
N1	65	32			0.015
N2-3	171	144			
Nx	93	0			
M stage					
M0	185	263			0.201
M1	1	7			
Mx	313	0			
NCCN stage					
I	25	18			
II	69	37			0.302
III	78	37			
IV	259	178			
Unknown	68	0			
Grade					
G1	61	NA			
G2	298	NA			NA
G3	119	NA			
G4	2	NA			
Unknown	19	NA			

Supplementary Table 5. Construction of the immune cell function (ICF) gene signature in HNSCC.

Supplementary Table 6. Comparisons of somatic variances between high- and low- risk groups.

Gene	Low-mutation (%)	Low-wild (%)	High-mutation (%)	High-wild (%)	P-value (chi-square test)
TP53	134 (54.7)	111 (45.3)	173 (70)	74 (30)	<0.001
TNN	81 (33.1)	164 (66.9)	91 (36.8)	156 (63.2)	0.379
FAT1	49 (20)	196 (80)	54 (21.9)	193 (78.1)	0.612
CDKN2A	44 (18)	201 (82)	44 (17.8)	203 (82.2)	0.966
MUC16	42 (17.1)	203 (82.9)	40 (16.2)	207 (83.8)	0.778
CSMD3	42 (17.1)	203 (82.9)	40 (16.2)	207 (83.8)	0.778
PIK3CA	39 (15.9)	206 (84.1)	40 (16.2)	207 (83.8)	0.934
NOTCH1	39 (15.9)	206 (84.1)	37 (15)	210 (85)	0.773
SYNE1	39 (15.9)	206 (84.1)	35 (14.2)	212 (85.8)	0.588
LRP1B	32 (13.1)	213 (86.9)	35 (14.2)	212 (85.8)	0.72
KMT2D	20 (8.2)	225 (91.8)	42 (17)	205 (83)	0.003
PCLO	27 (11)	218 (89)	32 (13)	215 (87)	0.509
NSD1	34 (13.9)	211 (86.1)	20 (8.1)	227 (91.9)	0.04
DNAH5	27 (11)	218 (89)	27 (10.9)	220 (89.1)	0.975
USH2A	29 (11.8)	216 (88.2)	22 (8.9)	225 (91.1)	0.286
FLG	22 (9)	223 (91)	27 (10.9)	220 (89.1)	0.47
CASP8	27 (11)	218 (89)	20 (8.1)	227 (91.9)	0.27

RYR2	20 (8.2)	225 (91.8)	22 (8.9)	225 (91.1)	0.768
PKHD1L1	17 (6.9)	228 (93.1)	25 (10.1)	222 (89.9)	0.207
XIRP2	25 (10.2)	220 (89.8)	15 (6.1)	232 (93.9)	0.094

Supplementary Table 7. Molecular docking results of the top 10 compounds.

Rank	ZINC ID	Compound name	Binding energy (kcal/mol)
1	ZINC000011679756	Eltrombopag	-8.3
2	ZINC000116473771	none	-8
3	ZINC000012503187	Conivaptan	-7.8
4	ZINC000003784182	Differin	-7.6
5	ZINC000052955754	Ergotamine	-7.5
6	ZINC000003945984	Vexol	-7.5
7	ZINC000003795819	Palonosetron	-7.4
8	ZINC000084668739	Lifitegrast	-7.4
9	ZINC000003875484	Androxy	-7.3
10	ZINC000064033452	Lumacaftor	-7.3

Supplementary Table 8. Genes in the black module of WGCNA.